THE MEGASECOND CHANDRA X-RAY VISIONARY PROJECT OBSERVATION OF NGC 3115. II. PROPERTIES OF POINT SOURCES

Dacheng Lin^{1,2}, Jimmy A. Irwin², Ka-Wah Wong³, Zachary G. Jennings⁴, Jeroen Homan⁵, Aaron J. Romanowsky^{4,6},

Jay Strader⁷, Gregory R. Sivakoff⁸, Jean P. Brodie⁴, and Ronald A. Remillard⁵

Space Science Center, University of New Hampshire, Durham, NH 03824, USA; dacheng.lin@unh.edu

Department of Scientific, Inc., 2452 Delmer Street Suite 100, Oakland, CA 94602-3017, USA

Huniversity of California Observatories, Santa Cruz, CA 95064, USA

MIT Kavli Institute for Astrophysics and Space Research, MIT, 70 Vassar Street, Cambridge, MA 02139-4307, USA

Department of Physics and Astronomy, San José State University, One Washington Square, San José, CA 95192, USA

Department of Physics and Astronomy, Michigan State University, East Lansing, Michigan, MI 48824, USA

Department of Physics, University of Alberta, Edmonton, Alberta, T6G 2E1, Canada

Received 2014 November 13; accepted 2015 May 16; published 2015 July 15

ABSTRACT

We carried out an in-depth study of low-mass X-ray binaries (LMXBs) detected in the nearby lenticular galaxy NGC 3115 using the Megasecond *Chandra* X-ray Visionary Project observation (total exposure time 1.1 Ms). In total we found 136 candidate LMXBs in the field and 49 in globular clusters (GCs) above 2σ detection, with 0.3–8 keV luminosity $L_{\rm X} \sim 10^{36} - 10^{39}\,{\rm erg\,s^{-1}}$. Other than 13 transient candidates, the sources overall have less long-term variability at higher luminosity, at least at $L_{\rm X} \gtrsim 2 \times 10^{37}\,{\rm erg\,s^{-1}}$. In order to identify the nature and spectral state of our sources, we compared their collective spectral properties based on single-component models (a simple power law or a multicolor disk) with the spectral evolution seen in representative Galactic LMXBs. We found that in the $L_{\rm X}$ versus photon index $\Gamma_{\rm PL}$ and $L_{\rm X}$ versus disk temperature $kT_{\rm MCD}$ plots, most of our sources fall on a narrow track in which the spectral shape hardens with increasing luminosity below $L_{\rm X} \sim 7 \times 10^{37}\,{\rm erg\,s^{-1}}$, but is relatively constant ($\Gamma_{\rm PL} \sim 1.5$ or $kT_{\rm MCD} \sim 1.5$ keV) above this luminosity, which is similar to the spectral evolution of Galactic neutron star (NS) LMXBs in the soft state in the *Chandra* bandpass. Therefore, we identified the track as the NS LMXB soft-state track and suggested sources with $L_{\rm X} \lesssim 7 \times 10^{37}\,{\rm erg\,s^{-1}}$ as a tolls in the soft state and those with $L_{\rm X} \gtrsim 7 \times 10^{37}\,{\rm erg\,s^{-1}}$ as Z sources. Ten other sources (five are transients) displayed significantly softer spectra and are probably black hole X-ray binaries in the thermal state. One of them (persistent) is in a metal-poor GC.

Key words: Galaxy: stellar content – globular clusters: general – X-rays: binaries – X-rays: individual (NGC 3115) *Supporting material*: machine-readable tables

1. INTRODUCTION

In a low-mass X-ray binary (LMXB), a neutron star (NS) or a stellar-mass black hole (BH) accretes matter from a Rochelobe filling, low-mass companion star via an accretion disk. Copious X-rays are produced in the inner disk (Shakura & Sunyaev 1973). In the case of NS LMXBs, there is also strong X-ray emission from the boundary layer formed by the settling of the accretion flow onto the NS surface (Inogamov & Sunyaev 1999; Popham & Sunyaev 2001). Our knowledge of LMXBs was revolutionized thanks to 16 years of intensive observations of such objects in our Galaxy by the *Rossi X-ray Timing Explorer (RXTE*; Bradt et al. 1993).

BH LMXBs constitute the majority of BH X-ray binaries (BHBs) known in our Galaxy, although a few BHBs with high-mass stellar companions also exist. BHBs exhibit three main X-ray spectral states: the hard state, the thermal state, and the steep power law (SPL) state (McClintock & Remillard 2006; Remillard & McClintock 2006). These states are normally described with spectral models consisting of two main continuum components: a standard thermal multicolor disk (MCD, diskbb in XSPEC, Arnaud 1996) and a Comptonized component (often modeled with a single power law, PL, or the Comptonization model compt in XSPEC). The hard state, which tends to occur below several percent of the Eddington luminosity ($L_{\rm Edd}$), is characterized by a strong Comptonized

component dominating the spectra at least above ~2 keV and extending to more than 100 keV. A weak, cool thermal disk might also be detected, with the maximum disk temperature $kT_{\rm MCD} \ll 1$ keV. The thermal state, which is normally observed at high luminosities, is characterized by a strong disk component with $kT_{\rm MCD}\sim 0.5$ -1 keV and the disk fraction of >75% in 2-10 keV (as defined in Remillard & McClintock 2006). A weak Comptonized component is also often present, but it only dominates at high energies. The SPL state tends to occur at very high luminosities ($\gtrsim 0.1 L_{\rm Edd}$), and the hallmark of this state is a strong Comptonizaton component with photon index $\Gamma_{PL} \sim 2.5$ (Remillard & McClintock 2006). A sizable thermal component is also normally seen in this state. Almost all known Galactic BH LMXBs are transient. They often show hysteresis in transitions to and from the hard state, with the transition to the hard state occuring at luminosities that are tightly clustered around 2% of the Eddington value (Maccarone 2003), and the transition from the hard state at higher but more scattered luminosities (Miyamoto et al. 1995; Maccarone & Coppi 2003; Homan & Belloni 2005). Similar hysteresis behavior is observed in transient NS LMXBs.

There are two main classes of NS LMXBs, atoll and Z sources (Hasinger & van der Klis 1989; van der Klis 2006, pp. 39–112), which are named after the patterns that they trace out in X-ray color–color diagrams (CDs) or hardness-intensity

diagrams (HIDs). Atolls radiate at $\sim 0.001-0.5$ $L_{\rm Edd}$ and trace out their patterns in CDs/HIDs on timescales of weeks to months. They have two main distinct spectral states: hard $(\Gamma_{PL} \lesssim 2$, extending to 100 keV or above) and soft (most emission $\lesssim 20 \text{ keV}$). The hard state tends to be observed at low luminosity ($\lesssim 0.1 L_{\rm Edd}$), while the soft state is normally observed at high luminosity (larger than a few percent L_{Edd}). Spectra in the transitional state between these two are also occasionally seen. Z sources are more luminous than atolls at near or above Eddington luminosity, and they trace out roughly Z-shaped tracks in CDs/HIDs within a few days (i.e., faster than atolls), with X-ray spectra that are generally soft. Thanks to a recent transient Z source, XTE J1701-462, which exhibited the Z-source characteristics when it was accreting at near or above Eddington luminosity and transitioned to an atoll during the decay of its 2006-2007 outburst, we now know that Z and atoll sources are essentially the same type of object at different mass accretion rates (Lin et al. 2009; Homan et al. 2010). Unlike BHBs, whose tracks for the thermal state in the CDs/HIDs tend to show large scatter, NS LMXBs tend to trace out clear narrow tracks in the soft state in the CDs/HIDs, which depend mostly on the accretion rate (Done & Gierliński 2003; Remillard & McClintock 2006; Fridriksson et al. 2015). Unlike BHBs, whose tracks in the CDs/HIDs tend to show large scatter, mainly due to the presence of the SPL state, NS LMXBs tend to trace out clear narrow tracks in the CDs/HIDs, which depend mostly on the accretion rate (Done & Gierliński 2003; Remillard & McClintock 2006; Fridriksson et al. 2015).

The spectral modeling for NS LMXBs is complicated by the presence of the boundary layer emission and is relatively controversial compared to BHBs. Lin et al. (2007) used a similar spectral model to the one used for BHBs (described earlier), except for an additional single-temperature blackbody (BB) to describe the boundary layer, and were able to infer L $\propto T^4$ trends for both the disk and the boundary layer in the soft state of two atolls. Such a trend for the disk is often observed for the thermal state of BHBs and is expected if the disk is essentially thermal and is truncated at the innermost stable circular orbit (ISCO). Lin et al. (2009) applied this model to XTE J1701–462 and also observed the $L \propto T^4$ trends for both the disk and the boundary layer in its atoll stage. However, such trends were not observed in its Z-source stage because the inner disk and the boundary layer both reach the local Eddington limit in this stage; thus the increase in the accretion rate tends to lead to an increase in the emission area with relatively constant temperature (increasing the inner disk radius at constant inner disk temperature for the accretion disk).

Our knowledge of the X-ray binaries in nearby galaxies has significantly increased since the launch of *XMM-Newton* and *Chandra X-ray Observatory* in 1999. In particular, *Chandra*'s superb spatial resolution and excellent sensitivity (Weisskopf et al. 2002) allow for population studies of X-ray binaries in a single galaxy with snapshots, which is important for understanding the origin and evolution of such sources. To fully understand these sources, one key task is to identify their nature (i.e., BH versus NS X-ray binaries) and the X-ray spectral state. To achieve this, early studies tried to stack sources in luminosity ranges in order to improve the statistics (Irwin et al. 2003; Maccarone et al. 2003). Recently, relatively detailed studies of individual sources in nearby galaxies were carried out (e.g., Brassington et al. 2010, 2012; Burke et al. 2013;

Barnard et al. 2013, 2014), but limited by statistics, these studies have been mostly focused on the few most luminous sources (above several $10^{37}\,\mathrm{erg\,s^{-1}}$) in each galaxy. It turns out that the differentiation between BH and NS X-ray binaries is generally very difficult. This is because most sources have X-ray spectra that are relatively hard ($\Gamma_{PL}<2.5$) in the *Chandra* and *XMM-Newton* bandpass (about 0.3–8 keV) and it is difficult to determine whether they are BHBs in the hard state or NS LMXBs in the soft state (they are unlikely to be NS LMXBs in the hard state due to the high luminosities of the sources studied). NS LMXBs in the soft state can appear hard in such an energy band because of the presence of the hot boundary layer component in the X-ray spectra (e.g., Lin et al. 2010, 2012a).

NGC 3115was selected as the target of a 1 Megasecond Chandra X-ray Visionary Project (XVP) in Cycle 13. The goals were to study the gas flow inside the Bondi radius of the central supermassive BH and obtain a deep look at the X-ray binary population of a normal early-type galaxy. The former has been presented in Wong et al. (2014). For the X-ray binaries, we presented the X-ray luminosity function in Lin et al. (2015, Paper III hereafter), and here we concentrate on the detailed properties of discrete sources, such as the longterm spectral and flux variability and the spectral characteristics. One main goal of our study is to identify their nature, but different from previous studies, we will achieve this by systematic comparison of our sources at various luminosity levels with Galactic X-ray binaries. NGC 3115 is a lenticular (S0) galaxy with an age of ~8.4 Gyr (Sánchez-Blázquez et al. 2006) and at a distance of 9.7 Mpc (Tonry et al. 2001). Including previous observations, the total exposure time of Chandra on this galaxy is ~1.1 Ms, and the limiting X-ray luminosity is $\sim 10^{36}$ erg s⁻¹, making it one of *Chandra*'s best observed normal early-type galaxies.

In Section 2, we describe the source detection, the calculation of flux, the simple spectral fits, the measurement of long-term and short-term variability, and multiwavelength cross-correlation. In Section 3, we present the various properties of X-ray binaries in NGC 3115, including the long-term variability and spectral characteristics that are used to classify the sources. We further discuss the possible nature of our sources in Section 4. We present our conclusions in Section 5.

2. DATA ANALYSIS

2.1. Observations and Source Detection

The 11 *Chandra* observations of NGC 3115 are listed in Table 1. They were made during three epochs: one in 2001, two in 2010, and nine in 2012. We hereafter refer to them as Obs 1–11 in chronological order (Table 1). All observations used the imaging array of the AXAF CCD Imaging Spectrometer (ACIS; Bautz et al. 1998). We analyzed the data with the *Chandra* Interactive Analysis of Observations (CIAO, version 4.6) package. We reprocessed the data to apply the latest calibration (CALDB 4.5.9) and the subpixel algorithm (Li et al. 2004) using the CIAO script *chandra_repro*. Background flares are only clearly seen in Obs 1, 5, and 6, for only very short durations. We excluded them if they are higher than 4σ above the mean background level. In this way, we excluded 1.2, 3.6, and 2.7 ks data for Obs 1, 5, and 6, respectively. The final exposure used for each observation is given in Table 1.

Table 1
Observation Log

Notation	Obs. ID	Date	Exposure (ks)	Offset ^a (arcmin)
1	2040	2001 Jun 14	35.8	1.5
2	11268	2010 Jan 27	40.6	0.1
3	12095	2010 Jan 29	75.6	0.1
4	13817	2012 Jan 18	171.9	0.0
5	13822	2012 Jan 21	156.6	0.0
6	13819	2012 Jan 26	72.9	0.0
7	13820	2012 Jan 31	184.1	0.0
8	13821	2012 Feb 03	157.9	0.0
9	14383	2012 Apr 04	119.4	0.3
10	14419	2012 Apr 05	46.3	0.3
11	14384	2012 Apr 06	69.7	0.3

Note.

To increase the detection sensitivity, we combined all 11 observations to create a deep merged observation (Obs *Esum* hereafter) using the CIAO script $merge_obs$. To correct for relative astrometry between the different observations, we created new aspect solution files by comparing the source list from each single observation to the source list from a single reference observation, which we chose to be the longest observation (13820). We only used bright sources ($>6\sigma$) with off-axis angles <6' in the cross-correlation. The average separation residuals of the source matches are 0''.1 after relative astrometry correction. The new aspect solution files were then applied to the event files and subsequent analysis.

We used the CIAO wavdetect wavelet-based source detection algorithm (Freeman et al. 2002) to search for discrete X-ray sources. The search was done twice, first over the single observations to determine the relative astrometry correction described above and the second time over the (relative astrometry corrected) single observations and the merged one. The count images were made in the broad (b) energy band 0.5-7.0 keV adopted in the Chandra Source Catalog, while the exposure maps were constructed at the corresponding monochromatic effective energy (i.e., 2.3 keV, Evans et al. 2010). The point-spread function (PSF) maps used correspond to the 50% enclosed counts fraction at 2.3 keV. For the merged observation, the PSF map was obtained by averaging those from single observations weighted by the exposure. We used two different resolutions: one at single sky pixel resolution (0".492) over the full field of view (FOV) and the other at 1/8 sky pixel resolution covering an area of $3' \times 3'$ centering at the center of NGC 3115. The subpixel binning images were used to improve the spatial resolution in the crowded field near the center of the galaxy. The limiting significance level was set to 10^{-6} , which formally corresponds to ~1 false source due to random fluctuations per 1024 × 1024 image pixels (about one CCD area for images at single sky pixel resolution). The wavelet scales were set to 1, 2, 4, 8, 16, and 32 image pixels for images at single sky pixel resolution, and 4, 8, 16, 32, 64, 128, and 256 image pixels for images at 1/8 sky pixel resolution.

Sources detected from the merged observation and single observations were cross-correlated to create the unique source list. Starting from the source list from the merged observation, we searched for new sources detected in single observations but not in the merged one. Such sources should be faint and highly

variable or transient. Sources are deemed to be duplicates if their separation is less than their combined 99.73% (i.e., 3σ) statistical positional uncertainty, or if their 50% PSF circular regions overlap with each other across different observations. The statistical positional uncertainties that we used are based on Equation (12) of Kim et al. (2007), which provides the 95% statistical positional uncertainty as a function of the source net counts and the off-axis angle based on a large number of simulations using the Chandra simulation tool MARX. The 95% positional uncertainties are converted to the 99.73% errors by multiplying by a factor of 1.405 (this assumed a twodimensional, circularly symmetric Gaussian distribution for the source position from wavdetect). As a check on the above matching criteria, we also tested a smaller searching radius by using the 95% statistical positional uncertainty only (the 50% PSF overlapping is not used). In the end, 95 more sources were found. From visual inspection, we found that six of them were in the central crowded field and two at the CCD edge, thus probably having large systematic positional uncertainties and explaining their relatively large offsets from detections from the merged observation. The remaining sources are generally separated from those of the merged observation much less than the size of their region ellipse from wavdetect. Thus in the end we did not treat any of these 95 sources as new sources and used the source list obtained above using the 99.73% statistical positional uncertainty and the 50% PSF circular region.

2.2. Flux and Spectral Characterization

After obtaining a merged source list, we extracted the spectrum for each source for each single observation. The source region was set to be a circle enclosing 90% of the PSF at 2.3 keV. The background region was set to be a concentric annulus, with inner and outer radii of two and five times the source radius, respectively. Nearby sources, if present, were excluded from the source and background regions, but the inner circular source region enclosing 50% of the PSF was not excluded. We used the CIAO task *mkacisrmf* to create the response matrix files and the CIAO tasks *mkarf* and *arfcorr* to create the point-source aperture-corrected auxiliary response files. The spectral and response files corresponding to the merged observation were created using the CIAO task *combine spectra*.

The background-subtracted count rates (but not aperture corrected) in different energy bands were obtained from the spectral files. To correctly determine confidence bounds for low count limits, we used the CIAO task *aprates*. The conversions from the count rates to the fluxes were based on the response files and assumed an absorbed PL spectral shape with $\Gamma_{PL}=1.7$ and Galactic absorption $N_{H}=4.32\times10^{20}\,\mathrm{cm^{-2}}$ (Kalberla et al. 2005). Throughout the paper, all fluxes and luminosities quoted (including those obtained from spectral fits described later) are corrected for Galactic absorption (but not intrinsic absorption, unless indicated otherwise).

To characterize the spectral properties of our sources, we calculated the hardness ratios HR = (H - S)/(H + S), where S and H are the energy fluxes in the soft and hard energy bands, respectively, using the method of Bayesian estimation (Park et al. 2006). We also carried out simple spectral fits to spectra above 4σ using two single-component models: a PL and an MCD. Due to the low statistics of most sources, we binned the spectra to have a minimum of one count per bin and used the C statistic in the fits. Both models included absorption (we used

^a Aim point offset from observation 13820.

the *wabs* model in XSPEC; we found no significant effect on our results if we chose other absorption models, such as *tbabs*, due to little absorption of most of our sources), with the minimum set to be the Galactic value of $N_{\rm H} = 4.32 \times 10^{20}$ cm⁻².

2.3. Long-term and Short-term Variability

The variability of the source was measured in several aspects. We defined the long-term flux variability as $V_{\rm var} = F_{\rm max}/F_{\rm min}$ and the significance of the difference as

$$S_{\text{var}} = \frac{F_{\text{max}} - F_{\text{min}}}{\left(\sigma_{\text{max}}^2 + \sigma_{\text{min}}^2\right)^{1/2}},\tag{1}$$

where $F_{\rm max}$ and $F_{\rm min}$ are the maximum and minimum 0.5–7.0 keV fluxes of a unique source among the single observations, with the corresponding errors $\sigma_{\rm max}$ and $\sigma_{\rm min}$, respectively. We only used detections with the flux above twice the error (σ) when calculating $F_{\rm max}$ (if no detections above 2σ , the one with the highest significance was used as $F_{\rm max}$); we used 2σ as the flux for detections with flux less than 2σ when calculating $F_{\rm min}$.

We measured the short-term variability using the Gregory–Loredo algorithm (Gregory & Loredo 1992) implemented by the CIAO tool *glvary* (Evans et al. 2010). It splits the events into multiple time bins and looks for significant deviations. The variation of the effective area with time was taken into account and was obtained by another CIAO tool: *dither_region*. The different degrees of confidence are indicated by the parameter of "variability index," which spans values within [0, 10] and is larger for a variability of higher confidence (Evans et al. 2010).

2.4. Multiwavelength Cross-correlation

Accompanying the *Chandra* XVP observation, a six pointing Hubble Space Telescope (HST) mosaic observation in the F475W and F850LP filters (hereafter g and z) using the Advanced Camera for Surveys (ACS) was also acquired in the field of NGC 3115. The total FOV of this mosaic observation is slightly larger than the D_{25} region of NGC 3115, which has a semimajor axis of a = 3'.62 (10.2 kpc), a semiminor axis of b = 1.23 (3.5 kpc), and a position angle of 40° (de Vaucouleurs et al. 1991). The galaxy was also imaged in g-, r-, and i-band filters on 2008 January 4 using Suprime-Cam on the 8.2 m Subaru telescope. In Paper III we cross-correlated our X-ray sources with the 360 globular clusters (GCs) from the HST/ACS mosaic imaging and the 421 ones from the Subaru/ Suprime-Cam imaging (Arnold et al. 2011; Jennings et al. 2014). The match was identified if the separation is less than the 99.73% positional uncertainty (combining the X-ray and optical components). The maximum separation allowed is 2" in order to limit the spurious rate. We note that before the cross-correlation, the systematic offset between different source lists was corrected through multiple steps: first the Subaru/ Suprime-Cam astrometry was registered to the USNO-B1.0 Catalog (Monet et al. 2003), then the HST/ACS astrometry was registered to the Subaru/Suprime-Cam catalog, and finally the astrometry of our X-ray sources was registered to the HST/ACS catalog (therefore the absolute astrometry of our X-ray sources has been corrected).

Table 2 lists the 37 matches with *HST*/ACS GCs (23 have the g-z color >1.13 and thus are red/metal-rich, while the

other 14 have g-z < 1.13 and are blue/metal-poor, following the division in Jennings et al. 2014) and the seven matches with Subaru/Suprime-Cam GCs identified in Paper III. In Paper III, we also identified five other sources whose optical counterparts were not classified as GCs by Jennings et al. (2014) but were assumed to be GC candidates by us (Table 2). Four of them (S12, S53, S65, and S79) are within $0.25D_{25}$, and thus very unlikely to be active galactic nuclei (AGNs; Paper III). The other one (S92), at an outer region, has an optical counterpart with the size and color typical of GCs, although it has a radial velocity from the spectroscopic measurement (238 km s⁻¹, Table 2) that is lower than typical values seen in other GCs (>350 km s⁻¹).

Adopting the same matching criteria, we also searched for the non-GC counterparts to our X-ray sources outside $0.25D_{25}$ from these optical observations. Such matches are most probably cosmic X-ray background sources (CXBs), especially AGNs, instead of the optical counterparts to field LMXBs. The optical emission of field LMXBs can achieve the maximum when the accretion rate is near the Eddington limit and the companion is an evolved star (so there is bright optical emission from both a large disk and a large companion), as seen in the Galactic Z source Cyg X-2 (van Paradijs & McClintock 1995). However, such sources are still below the detection limit of our optical images by ~3 mag. By rotating the X-ray source positions around the center of the galaxy by $\pm 10^{\circ}$, $\pm 170^{\circ}$, and 180° , and using X-ray sources above 4σ , we estimated the rate of spurious matches to be about 3% and 5% for the HST/ACS counterparts and Subaru/Suprime-Cam matches, respectively.

From visual inspection, we found that some very faint sources in the HST/ACS observation were not detected by the tool SExtractor used by Jennings et al. (2014). Concentrating on the region within $(0.25-1)D_{25}$, we visually identified five X-ray sources that are coincident with such faint sources and assume them to be AGNs. Within $0.25D_{25}$, we also visually found one source (i.e., S65) with a faint counterpart not detected by Jennings et al. (2014), and we assumed it to be a GC, as mentioned.

3. RESULTS AND DISCUSSION

3.1. The Source List and Identification

Figure 1 shows the false-colored *Chandra* X-ray image of NGC 3115. We detected 525 unique sources from the merged and single observations. After eliminating sources below 2σ (i.e., the net counts within the 90% PSF region divided by the error less than two), we are left with 490 sources. We found that the ACIS-S1 chip, which is well outside the galaxy (>3 D_{25}), shows some bright streaks, especially at energies \lesssim 0.7 keV. We eliminated seven sources detected in such streaks, as they are most probably spurious. We also eliminated another source with probably spurious large variability due to being at the CCD edge. In the end we have 482 sources in total.

Table 3 gives the various properties of the sources, such as the flux, the long-term variability, and the maximum Gregory–Loredo variability index. We also give some source type information. The sources within D_{25} are expected to be dominated by LMXBs and are thus assumed to be such objects, except those with non-GC optical counterparts, which we identify as AGNs. The LMXBs identified in this way are expected to be contaminated by some AGNs, because our

Table 2
The GC LMXBs and Candidates

$ \begin{array}{cccccccccccccccccccccccccccccccccccc$	$(mag) \\ (8)$ 18.968 ± 0.003 22.414 ± 0.046 20.274 ± 0.116 20.631 ± 0.183 21.821 ± 0.031 19.644 ± 0.005 20.633 ± 0.010 19.854 ± 0.239 19.217 ± 0.004 20.336 ± 0.011 19.174 ± 0.004 20.484 ± 0.009 19.205 ± 0.023 18.992 ± 0.003	(pc) (9) 2.49 0.94 1.30 1.36 0.77 1.91 2.23 2.59 2.47 2.42 1.76 1.22	(km s ⁻¹) 1123 456 696 407 821 697
$\begin{array}{cccccccccccccccccccccccccccccccccccc$	$\begin{array}{c} 22.414 \pm 0.046 \\ 20.274 \pm 0.116 \\ 20.631 \pm 0.183 \\ 21.821 \pm 0.031 \\ 19.644 \pm 0.005 \\ \dots \\ 20.633 \pm 0.010 \\ 19.854 \pm 0.239 \\ \dots \\ 19.217 \pm 0.004 \\ 20.336 \pm 0.011 \\ 19.174 \pm 0.004 \\ \dots \\ 20.484 \pm 0.009 \\ 19.205 \pm 0.023 \\ \end{array}$	0.94 1.30 1.36 0.77 1.91 2.23 2.59 2.47 2.42 1.76 1.22	 456 696 407 821 697
$\begin{array}{cccccccccccccccccccccccccccccccccccc$	$\begin{array}{c} 20.274 \pm 0.116 \\ 20.631 \pm 0.183 \\ 21.821 \pm 0.031 \\ 19.644 \pm 0.005 \\ \dots \\ 20.633 \pm 0.010 \\ 19.854 \pm 0.239 \\ \dots \\ 19.217 \pm 0.004 \\ 20.336 \pm 0.011 \\ 19.174 \pm 0.004 \\ \dots \\ 20.484 \pm 0.009 \\ 19.205 \pm 0.023 \\ \end{array}$	1.30 1.36 0.77 1.91 2.23 2.59 2.47 2.42 1.76 1.22	456 696 407 821 697
$\begin{array}{cccccccccccccccccccccccccccccccccccc$	$\begin{array}{c} 20.631 \pm 0.183 \\ 21.821 \pm 0.031 \\ 19.644 \pm 0.005 \\ \dots \\ 20.633 \pm 0.010 \\ 19.854 \pm 0.239 \\ \dots \\ 19.217 \pm 0.004 \\ 20.336 \pm 0.011 \\ 19.174 \pm 0.004 \\ \dots \\ 20.484 \pm 0.009 \\ 19.205 \pm 0.023 \\ \end{array}$	1.36 0.77 1.91 2.23 2.59 2.47 2.42 1.76 1.22	 696 407 821 697
$\begin{array}{cccccccccccccccccccccccccccccccccccc$	21.821 ± 0.031 19.644 ± 0.005 20.633 ± 0.010 19.854 ± 0.239 19.217 ± 0.004 20.336 ± 0.011 19.174 ± 0.004 20.484 ± 0.009 19.205 ± 0.023	0.77 1.91 2.23 2.59 2.47 2.42 1.76 1.22	 696 407 821 697
$\begin{array}{cccccccccccccccccccccccccccccccccccc$	$\begin{array}{c} 19.644 \pm 0.005 \\ \dots \\ 20.633 \pm 0.010 \\ 19.854 \pm 0.239 \\ \dots \\ 19.217 \pm 0.004 \\ 20.336 \pm 0.011 \\ 19.174 \pm 0.004 \\ \dots \\ 20.484 \pm 0.009 \\ 19.205 \pm 0.023 \\ \end{array}$	1.91 2.23 2.59 2.47 2.42 1.76 1.22	696 407 821 697
$\begin{array}{cccccccccccccccccccccccccccccccccccc$	$\begin{array}{c} \dots \\ 20.633 \pm 0.010 \\ 19.854 \pm 0.239 \\ \dots \\ 19.217 \pm 0.004 \\ 20.336 \pm 0.011 \\ 19.174 \pm 0.004 \\ \dots \\ 20.484 \pm 0.009 \\ 19.205 \pm 0.023 \\ \end{array}$	2.23 2.59 2.47 2.42 1.76 1.22	 407 821 697
$\begin{array}{cccccccccccccccccccccccccccccccccccc$	20.633 ± 0.010 19.854 ± 0.239 19.217 ± 0.004 20.336 ± 0.011 19.174 ± 0.004 20.484 ± 0.009 19.205 ± 0.023	2.23 2.59 2.47 2.42 1.76 1.22	407 821 697
$\begin{array}{cccccccccccccccccccccccccccccccccccc$	19.854 ± 0.239 19.217 ± 0.004 20.336 ± 0.011 19.174 ± 0.004 20.484 ± 0.009 19.205 ± 0.023	2.59 2.47 2.42 1.76 1.22	 821 697
$\begin{array}{cccccccccccccccccccccccccccccccccccc$	$$ 19.217 ± 0.004 20.336 ± 0.011 19.174 ± 0.004 $$ 20.484 ± 0.009 19.205 ± 0.023	2.59 2.47 2.42 1.76 1.22	 821 697
$\begin{array}{cccccccccccccccccccccccccccccccccccc$	19.217 ± 0.004 20.336 ± 0.011 19.174 ± 0.004 20.484 ± 0.009 19.205 ± 0.023	2.47 2.42 1.76 1.22	821 697
$\begin{array}{cccccccccccccccccccccccccccccccccccc$	20.336 ± 0.011 19.174 ± 0.004 20.484 ± 0.009 19.205 ± 0.023	2.42 1.76 1.22	821 697
$\begin{array}{cccccccccccccccccccccccccccccccccccc$	$19.174 \pm 0.004 \\ \dots \\ 20.484 \pm 0.009 \\ 19.205 \pm 0.023$	1.76 1.22	697
$\begin{array}{cccccccccccccccccccccccccccccccccccc$	$ 20.484 \pm 0.009 19.205 \pm 0.023$	1.22	
$\begin{array}{cccccccccccccccccccccccccccccccccccc$	$\begin{array}{c} 20.484 \pm 0.009 \\ 19.205 \pm 0.023 \end{array}$		
$\begin{array}{cccccccccccccccccccccccccccccccccccc$	19.205 ± 0.023		
121 A10 0.07 20.310 \pm 0.003 19.148 \pm 0.004 20.138 \pm 0.028 19.457 \pm 0.030 129 A2 0.13 19.928 \pm 0.002 18.752 \pm 0.002 19.989 \pm 0.003 19.308 \pm 0.004	19.205 ± 0.023	2.17	
129 A2 0.13 19.928 \pm 0.002 18.752 \pm 0.002 19.989 \pm 0.003 19.308 \pm 0.004		2.42	
		1.69	
135 A29 0.21 20.981 ± 0.005 20.055 ± 0.006 21.044 ± 0.008 20.412 ± 0.009	20.225 ± 0.009	1.84	
145 A57 0.10 21.923 \pm 0.006 20.488 \pm 0.004 22.024 \pm 0.010 21.233 \pm 0.010	20.875 ± 0.009	1.08	798
150 A33 0.13 21.067 \pm 0.004 20.084 \pm 0.004 21.074 \pm 0.007 20.454 \pm 0.008	20.252 ± 0.008	2.30	949
153 A5 0.06 20.033 \pm 0.002 18.802 \pm 0.002 20.091 \pm 0.004 19.360 \pm 0.004	19.062 ± 0.003	1.74	682
171 A14 0.03 20.595 \pm 0.003 19.468 \pm 0.002 20.623 \pm 0.004 19.924 \pm 0.005	19.660 ± 0.004	1.57	
183 A63 0.06 21.549 \pm 0.005 20.585 \pm 0.005 21.584 \pm 0.008 20.958 \pm 0.009	20.745 ± 0.009	1.84	441
187 A99 0.11 22.531 \pm 0.010 20.975 \pm 0.006 21.507 \pm 0.013 21.679 \pm 0.014	21.292 ± 0.013	2.12	609
188 A13 0.03 20.434 \pm 0.003 19.424 \pm 0.003 20.394 \pm 0.004 19.747 \pm 0.005	19.513 ± 0.004	1.24	426
192 A262 0.03 23.616 \pm 0.022 22.202 \pm 0.019 23.671 \pm 0.034 22.909 \pm 0.040	22.530 ± 0.041	1.24	
200 A17 0.07 20.862 \pm 0.003 19.552 \pm 0.003 20.767 \pm 0.005 20.003 \pm 0.005	19.692 ± 0.005	2.54	439
212 A102 0.01 21.873 ± 0.006 21.002 ± 0.006 21.838 ± 0.008 21.285 ± 0.010	21.111 ± 0.010	2.56	
213 A232 0.15 22.836 \pm 0.011 21.887 \pm 0.011 22.913 \pm 0.018 22.303 \pm 0.022	22.103 ± 0.023	1.44	885
$\frac{22.305 \pm 0.011}{21.469 \pm 0.008}$ $\frac{22.905 \pm 0.011}{21.469 \pm 0.008}$ $\frac{22.905 \pm 0.016}{22.178 \pm 0.018}$	21.843 ± 0.017	1.10	750
219 A339 0.09 24.323 \pm 0.036 23.173 \pm 0.035 24.557 \pm 0.059 23.568 \pm 0.058	23.520 ± 0.071		
223 A32 0.08 21.179 \pm 0.004 20.080 \pm 0.004 21.235 \pm 0.006 20.548 \pm 0.007	20.297 ± 0.007	1.44	706
$\begin{array}{cccccccccccccccccccccccccccccccccccc$	20.237 ± 0.007 20.113 ± 0.006	2.37	809
$\begin{array}{cccccccccccccccccccccccccccccccccccc$	20.113 ± 0.000 22.999 ± 0.046	2.51	
225 A257 0.04 25.690 \pm 0.020 22.397 \pm 0.025 25.895 \pm 0.005 25.498 \pm 0.032 285 A249 0.37 22.933 \pm 0.013 22.051 \pm 0.016 22.935 \pm 0.019 22.393 \pm 0.024	22.185 ± 0.025	2.54	
289 A18 0.15 20.981 \pm 0.004 19.641 \pm 0.003 20.877 \pm 0.005 20.109 \pm 0.005	19.805 ± 0.005	2.37	881
259 A18 0.13 20.981 \pm 0.004 19.041 \pm 0.003 20.877 \pm 0.003 20.109 \pm 0.003 358 A192 0.97 22.516 \pm 0.008 21.628 \pm 0.008 22.528 \pm 0.012 22.044 \pm 0.016	21.797 ± 0.015	4.78	618
199 S624 0.12 22.176 ± 0.010 21.403 ± 0.010	21.051 ± 0.009		
322 S570 0.05 23.990 ± 0.031 23.158 ± 0.032	22.797 ± 0.029		
325 S454 0.64 22.852 ± 0.015 22.257 ± 0.018	21.991 ± 0.016		
332 S578 0.53 22.729 ± 0.014 21.953 ± 0.015	21.597 ± 0.013		
356 S364 0.64 22.867 ± 0.015 22.105 ± 0.016	21.814 ± 0.015		782
378 S664 0.59 22.220 ± 0.010 21.631 ± 0.012	21.379 ± 0.011		
451 S638 0.87 19.568 ± 0.003 18.802 ± 0.003	18.498 ± 0.003	•••	
12 0.06 23.377 ± 0.045 21.832 ± 0.042	•••	0.25	
53 \cdots 0.02 21.751 \pm 0.062 20.378 \pm 0.069 \cdots	•••	1.43	•••
79 0.03 21.053 ± 0.033 19.678 ± 0.033	•••	1.01	
92 ··· 0.07 21.693 ± 0.006 20.306 ± 0.005 21.738 ± 0.011 20.959 ± 0.011	20.608 ± 0.010	1.66	238

Note. Columns: (1) master source unique index; (2) GC in Jennings et al. (2014); (3) the offset between the GC center and our X-ray source; (4) *HST*/ACS *g*-band magnitude; (5) *HST*/ACS *z*-band magnitude; (6) SCam *g*-band magnitude; (7) SCam *r*-band magnitude; (8) SCam *i*-band magnitude; (9) half-light radius; (10) heliocentric velocity, if available, from the Pota et al. (2013) catalog. The top group includes 37 LMXBs coincident with *HST*/ACS GCs. The middle group includes seven LMXBs coincident with GCs detected/covered only in the Subaru/Suprime-Cam images, but not in the *HST*/ACS images. The bottom group includes four GC LMXB candidates whose optical matches were not classified as GCs by Jennings et al. (2014) but were assumed to be GCs by us (there is another similar source, S65, which is not included in the table because the photometry is not available due to being too close to the bright galaxy center; see the text for details). Our GC LMXB list is slightly different from that in Jennings et al. (2014), mainly because of our exclusion of very faint X-ray sources (<2\sigma) and update of calibration in our X-ray analysis.

optical images are not very deep. Limiting to the 137 relatively bright sources with $L_{\rm X,max}\gtrsim 4\times 10^{36}\,{\rm erg\,s^{-1}}$ (i.e., flux $\gtrsim 3.6\times 10^{-16}\,{\rm erg\,s^{-1}\,cm^{-2}})$ within D_{25} , which are the main

targets of this paper, we identify nine AGNs. As we found in Paper III, the CXB density in our field is consistent with the average value of Georgakakis et al. (2008) to within 20%, so

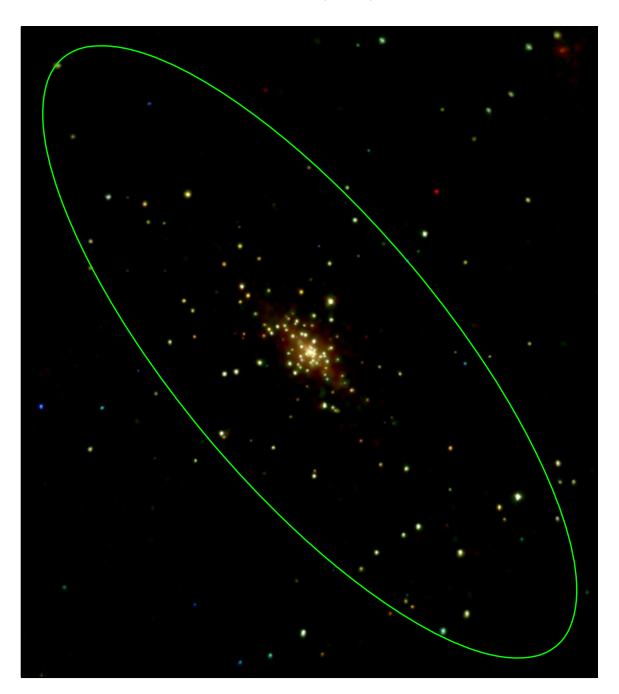


Figure 1. Chandra X-ray image of NGC 3115. The image is false-colored using adaptively smoothed (with the CIAO task csmooth), exposure corrected images in 0.5–1.2 keV (red), 1.2–2 keV (green), and 2–7 keV (blue). The D_{25} ellipse of the galaxy is also shown. The diffuse emission near the galaxy center comes from diffuse hot gas, unresolved LMXBs, and other unresolved stellar emission (Wong et al. 2011; Wong et al. 2014).

we expect <16.8 AGNs. Thus the number of AGNs that we might miss is \lesssim 8, which is negligibly small for our purposes. Sources outside D_{25} should be dominated by AGNs, because we only expect 1.5 field LMXBs above $4 \times 10^{36} \,\mathrm{erg \, s^{-1}}$ based on the IR light in the K_s band outside D_{25} (Paper III). Therefore, we assumed all sources outside D_{25} to be AGNs, except those coincident with GCs, the supersoft X-ray source (SSS) S109, three coronally active stars in our Galaxy (which are coincident with stars and show soft X-ray spectra and possible stellar flares), two galaxies (due to hot gas emission in galaxies; which are coincident with galaxies in the optical images and show soft X-ray spectra), and BHC S179 (Sections 3.2 and 3.3.2; it is slightly outside D_{25} but is also identified as a field LMXB, considering its possible transient nature and soft spectra). In total we have 136 candidate field LMXBs and 49 candiate GC LMXBs (Table 2). We also marked the 13 transients and 10 BH X-ray binary candidates (BHCs) in the source type column. Their identification will be described in the following sections.

Table 4 gives the counts, fluxes and hardness ratios of our sources in various energy bands in the merged observation (as well as the high-state and low-state observations for transients identified in the next section). The counts and fluxes of our sources in various energy bands in single observations are given in Table 5.

3.2. Long-term Variability

The observations of NGC 3115 by *Chandra* span more than a decade, which is ideal for investigating the long-term variability of LMXBs. Figure 2 shows the dependence of the long-term variability $V_{\rm var}$ on the maximum 0.5–7 keV luminosity $L_{\rm X,max}$ for all candidate LMXBs except those (24) within

the central elliptical region with semimajor axis a = 10'' and eccentricity and position angle following the D_{25} ellipse (this region is too crowded and the source extraction is subject to large systematic errors). We find that except for some transients (triangles, see below), V_{var} generally decreases with $L_{X,\text{max}}$ for bright GC and field LMXBs with $L_{\rm X,max} \gtrsim 2 \times 10^{37}\,{\rm erg\,s^{-1}}$. At lower luminosities, $V_{\rm var}$ seems to increase with $L_{\rm X,max}$, especially for field LMXBs. However, this is most probably artificial due to the detection limit of the observations; most of these sources have a minimum luminosity less than 2σ and we calculated their V_{var} using the 2σ upper limit of the minimum luminosity. Some GCs might contain multiple LMXBs (Paper III), but considering that we detect variability for all GC LMXBs, such source blending effects should not be significant. The long-term stability of the most luminous sources that we see in NGC 3115 is also seen in other galaxies (e.g., Irwin 2006).

To search for transients (i.e., quiescent sources with a single outburst) we concentrated on the 152 sources that are either within $2D_{25}$ (including those within the central a = 10''eclipse) or coincide with GCs and have at least one detection above 4σ . If we require transients to have $V_{\text{var}} \ge 5$ (there are 25) such sources), be hardly detected (with fluxes $<2\sigma$) in all observations in at least one epoch, and have the long-term light curve consistent with a global outburst (instead of an irregular, large variation), we are left with 13 candidates. We note that we did not use a very strict condition on the variability to select transients, as some persistent Galactic LMXBs are known to vary by factors of >10 (e.g., Homan et al. 2009; Maccarone et al. 2010). Therefore, we cannot rule out that some transient candidates we found might be just highly variable persistent sources. We plot the long-term light curves of the transient candidates in the left panels in Figures 3(a)-(d). There are three active in the first epoch (Figure 3(a)), one in the second epoch (Figure 3(b)), six in the third epoch (Figure 3(c)), and three active in both the second and the third epoch (Figure 3(d)). We note that S36 (Figure 3(c)), was bright in the third epoch but seems to show some emission in the first two epochs, making it not formally a good transient candidate, but this might be due to extended emission near the galactic center. We also note that only S8 and S103 are coincident with GCs.

As most of our observations were made within three months in the third epoch, only outbursts in this epoch are relatively well monitored. Among the six transient candidates that were active only in the third epoch (Figure 3(c)), three (S103, S125, and S198) clearly showed flux evolution during the outburst. We probably detected the decay of the outburst for S103 and S125. For S198 we had relatively good coverage of the outburst, including the rise, peak, and decay. Moreover, for S198, we caught a fast rise (<6 days), as commonly seen in X-ray binaries (Chen et al. 1997). These outbursts over monthlong timescales are typical for transient X-ray binaries. For the other three sources (S8, S26, and S36), the flux remained fairly steady in all seven observations in the third epoch, indicating relatively long outbursts (probably years).

The three transient candidates that were active in the second and third epochs had fairly steady fluxes in these two epochs. Because the second and third epochs together span \sim 2.2 years, which is much longer than the typical durations of outbursts seen in X-ray binaries (several months), these sources were experiencing prolonged outbursts. Such sources are rare but not

Table 3
The Master Source Catalog

Source	CXOU Name	PU	α/R_{25}	$L_{ m X,max}$	S/N	$V_{ m var}$	G-L _{max}	Туре
(1)	(2)	(3)	(4)	(5)	(6)	(7)	(8)	(9)
78	J100515.4-074254	0.05	0.168	7.41e+37	20.3	9.2	1	F, BH
96	J100516.2-074235	0.05	0.230	4.33e+37	19.5	1.7	2	GC, BH
97	J100514.2-074233	0.05	0.279	5.41e+37	19.0	2.6	7	F, BH
100	J100517.1-074217	0.07	0.323	2.67e+37	13.3	2.1	2	F, BH
104	J100516.5-074207	0.06	0.344	6.40e+37	19.1	4.0	2	F, BH
108	J100518.5-074138	0.06	0.518	1.27e+38	19.3	1.3	0	F, BH
179	J100510.9-074533	0.18	1.040	4.83e+37	6.2	19.8	1	F, BH, T
181	J100510.0-074529	0.15	0.936	1.71e+38	7.9	126.9	3	F, BH, T
193	J100508.7-074443	0.28	0.571	3.99e+37	2.9	30.1	1	F, BH, T
198	J100506.7-074433	0.08	0.711	1.17e+38	20.2	33.8	1	F, BH, T
8	J100517.2-074352	0.05	0.913	1.60e+38	37.2	54.8	2	GC, T
25	J100516.7-074317	0.04	0.532	1.88e+38	42.6	1.5	2	F
35	J100515.8-074312	0.04	0.349	2.10e+38	37.1	40.4	2	F, T
68	J100513.7-074300	0.03	0.078	2.28e+38	46.7	1.5	0	F
200	J100506.0-074428	0.06	0.808	5.71e+38	69.2	1.4	0	GC
212	J100527.3-074316	0.07	2.234	4.85e+38	57.7	1.4	2	GC

Note. A portion is shown here, using 10 BHCs (the top group) and six bright candidate NS LMXBs (the bottom group), for guidance regarding its form and content. Columns: (1) master source unique index; (2) IAU name (following the convention of CXOU Jhhmmss.s+/-ddmmss); (3) 1σ statistical positional uncertainty (in units of arcsec) in each coordinate, based on Equation (12) of Kim et al. (2007); (4) The ratio of the angular offset from the galaxy center to the elliptical radius of the D_{25} isophotal ellipse in the direction from the galaxy center to the source; (5) 0.5–7 keV maximum luminosity (in units of erg s⁻¹, assuming a source distance of 9.7 Mpc); (6) the signal-to-noise ratio (the 0.5–7 keV net counts divided by the error); (7) long-term variability; (8) the maximum Gregory–Loredo short-term variability index among different observations; and (9) the source type (field LMXB ("F"), GC LMXB ("GC"), transient ("T"), BHC ("BH"), star, AGN, galaxy ("G"), and SSS).

(This table is available in its entirety in machine-readable form.)

unique; several sources are known to have outbursts lasting for years to more than a decade (McClintock & Remillard 2006, pp. 157–213; Galloway et al. 2007; Soleri et al. 2010; Lin et al. 2014).

The sample spectra of all the transient candidates are shown in the right panels of Figure 3. Because of large variability of these sources and in order to increase the statistics, we combined observations with similar flux levels, as noted in the figure. The spectra shown generally represent the high state of the sources, except S198, for which we also created a low-state spectrum. While most spectra appear hard and we show the fits with a PL, some spectra seem soft (e.g., S179), and we show the fits with an MCD. As will be shown in the next section, these soft sources are most probably BHBs in the thermal state. We will discuss the spectral evolution and physical implication of S198 separately in Section 3.4.1.

3.3. X-Ray Spectral Properties

3.3.1. The Hardness Ratios

Figure 4 shows the luminosity versus hardness ratio diagram for our candidate LMXBs, obtained from the merged observation (or the merged high-state and low-state observations for transients). We separate the GC (left panel) and field (right panel) sources. For the former, we further differentiate different subgroups: the *HST*/ACS blue/metal-poor GCs in blue squares, the *HST*/ACS red/metal-rich GCs in red diamonds, and the Subaru/Suprime-Cam GCs and the extra five *HST*/ACS GC candidates identified by us (Section 2.4) in green circles. We observe no clear spectral differences between the different groups of GC LMXBs, which is in agreement with previous findings (e.g., Kim et al. 2006). For both GC and field populations, we find that other than a few very soft or very hard

outliers, our sources seem to follow a global trend that the luminous sources ($\geqslant 7 \times 10^{37} \, \mathrm{erg \ s^{-1}}$) have hard spectra consistent with $\Gamma_{PL} \sim 1.5$, while the fainter sources have systematically softer spectra. In the following sections we present more detailed source spectral properties based on simple spectral fits and provide systematic comparison with Galactic LMXBs, which allows us to shed more light on the nature of our sources and the cause of their spectral evolution.

3.3.2. Spectral Fits of Field LMXBs

The results of simple PL and MCD fits to the merged spectra (for transients, see Figure 3 for the spectra used) of candidate LMXBs are given in Table 6. The C statistic that we adopted in the fits does not indicate the fitting quality, but based on bright spectra that were rebinned to have a minimum of 20 counts per bin and fitted with the χ^2 statistic, we found that the fits are mostly acceptable with the reduced χ^2 <1.2 and the null hypothesis probability $\gtrsim 10\%$. There are a few relatively bad fits using the MCD model, with the reduced χ^2 of 1.4–1.7 and the null hypothesis probability of 10^{-2} – 10^{-4} . Because we are mostly interested in using the PL and MCD fits to roughly characterize the spectral shapes, the fitting quality overall is sufficient for our purposes.

The PL fits are shown in Figure 5, with the $0.3-8 \text{ keV } L_{\text{X}}$ versus Γ_{PL} in the top panels and N_{H} versus Γ_{PL} in the bottom panels; the MCD fits are shown in Figure 6, with L_{X} versus kT_{MCD} in the top panels and N_{H} versus kT_{MCD} in the bottom panels. The GC and field LMXBs are plotted separately, with GCs in the left panels and field LMXBs in the middle panels. In Figure 6, some dotted reference lines are included to show the expected dependence of the $0.3-8 \text{ keV } L_{\text{X}}$ luminosity on kT_{MCD} from the standard thermal disk truncated at the ISCO of

 Table 4

 The Source Counts, Flux, and Hardness Ratio in the Merged Observation

Source	Obs	Expo	C _b	$C_{\rm b}^1$	C _b ^u	F _b	$F_{\rm b}^{\rm l}$	F _b ^u	HR ₃	HR ₃	HR ₃ ^u
(1)	(2)	(3)	(4)	(5)	(6)	(7)	(8)	(9)	(10)	(11)	(12)
78	0	1131.0	418.4	397.8	439.2	3.36e-15	3.20e-15	3.53e-15	-0.19	-0.24	-0.14
96	0	1131.0	385.9	366.1	405.9	3.16e-15	3.00e-15	3.32e-15	-0.23	-0.28	-0.18
97	0	1131.0	363.2	344.1	382.5	2.96e-15	2.81e-15	3.12e-15	-0.34	-0.39	-0.29
100	0	1131.0	181.8	168.1	195.6	1.47e-15	1.36e-15	1.58e-15	-0.53	-0.60	-0.47
104	0	1131.0	366.1	346.9	385.5	2.96e-15	2.81e-15	3.12e-15	-0.19	-0.24	-0.13
108	0	443.2	367.1	348.0	386.3	9.98e-15	9.46e-15	1.05e-14	-0.27	-0.32	-0.22
179	0	1131.0	50.1	42.0	58.2	4.40e-16	3.70e-16	5.11e-16	-0.45	-0.59	-0.33
179	h	116.3	45.2	38.6	52.3	3.51e-15	3.00e-15	4.07e-15	-0.43	-0.58	-0.32
181	0	1131.0	73.3	64.0	82.7	6.79e-16	5.93e-16	7.66e-16	-0.18	-0.30	-0.07
181	h	35.8	74.9	66.3	83.6	1.51e-14	1.34e-14	1.69e-14	-0.06	-0.18	0.05
193	0	1061.3	13.8	9.0	19.2	1.30e-16	8.50e-17	1.80e-16	-0.05	-0.33	0.20
193	h	35.8	17.5	13.5	22.1	3.54e-15	2.74e-15	4.46e-15	-0.14	-0.41	0.07
198	0	1131.0	413.1	392.6	433.8	3.82e-15	3.63e-15	4.01e-15	-0.19	-0.25	-0.14
198	h	414.9	393.2	373.5	413.2	9.68e-15	9.19e-15	1.02e-14	-0.16	-0.22	-0.11
198	1	564.0	22.5	17.4	28.2	3.98e-16	3.08e-16	5.00e-16	-0.77	-0.94	-0.68
8	0	1131.0	1370.0	1333.2	1407.2	1.10e-14	1.07e-14	1.13e-14	-0.05	-0.09	-0.02
8	h	978.9	1370.8	1334.0	1407.9	1.30e-14	1.26e-14	1.33e-14	-0.07	-0.10	-0.03
25	0	1131.0	1789.1	1747.1	1831.5	1.44e-14	1.40e-14	1.47e-14	-0.09	-0.12	-0.06
35	0	1131.0	1356.0	1319.5	1393.0	1.10e-14	1.07e-14	1.13e-14	-0.10	-0.13	-0.06
35	h	978.9	1144.2	1110.6	1178.2	1.09e-14	1.06e-14	1.12e-14	-0.10	-0.13	-0.06
68	0	1131.0	2186.4	2139.7	2233.7	1.76e-14	1.72e-14	1.80e-14	-0.13	-0.16	-0.11
200	0	1131.0	4716.3	4648.2	4785.1	4.34e-14	4.28e-14	4.40e-14	0.00	-0.02	0.02
212	0	1130.8	3280.4	3223.5	3337.8	3.45e-14	3.39e-14	3.51e-14	-0.04	-0.06	-0.01

Note. A portion is shown here, using 10 BHCs (the top group) and six bright candidate NS LMXBs (the bottom group), for guidance regarding its form and content. Columns: (1) master source unique index; (2) observation ("0" refers the combination of all available observations; "h" refers to the combination of the high-state observations for the 13 transients, as shown in Figures 3(a)–(d); and "l" refers to the combination of the low-state observations for source 198, as shown in Figure 3(c)); (3) exposure time, in units of ks; (4–6) the net counts in the broad band (0.5-7.0 keV) and the lower and upper limits; (7–9) the energy flux in the broad band and the lower and upper limits in units of erg s⁻¹ cm⁻²; and (10–12) the hardness ratio using the fluxes in the 0.5–2.0 keV and 2.0–7.0 keV energy bands and the lower and upper limits. All limits are at the 68% confidence level.

(This table is available in its entirety in machine-readable form.)

Table 5
The Source Counts and Flux in Individual Observations

Source	ObsID	C_{b}	$C_{\rm b}^1$	$C_{\mathrm{b}}^{\mathrm{u}}$	F_{b}	$F_{ m b}^{ m l}$	$F_{\rm b}^{ m u}$
(1)	(2)	(3)	(4)	(5)	(6)	(7)	(8)
78	13820	86.9	77.6	96.4	4.37e-15	3.90e-15	4.84e-15
96	13820	49.0	42.2	56.5	2.47e-15	2.13e-15	2.85e-15
97	13820	56.0	48.5	63.5	2.82e-15	2.44e-15	3.20e-15
100	13820	32.1	26.6	38.1	1.60e-15	1.33e-15	1.91e-15
104	13820	38.6	32.5	45.2	1.93e-15	1.63e-15	2.26e-15
179	13820	0.7	0.0	2.8	3.78e-17	0	1.46e-16
181	13820	0.0	0.0	1.1	0	0	5.97e-17
193	13820	0.0	0.0	1.1	0	0	5.87e-17
198	13820	174.9	161.7	188.2	1.04e-14	9.60e-15	1.12e-14
8	13820	237.2	221.9	252.7	1.19e-14	1.12e-14	1.27e-14
25	13820	294.4	277.4	311.7	1.48e-14	1.39e-14	1.56e-14
35	13820	200.9	186.8	215.1	1.09e-14	1.01e-14	1.17e-14
68	13820	366.4	347.2	385.7	1.84e-14	1.75e-14	1.94e-14
200	13820	707.1	680.7	733.7	4.23e-14	4.08e-14	4.39e-14
212	13820	461.3	439.9	482.8	3.17e-14	3.02e-14	3.31e-14

Note. A portion is shown here, using 10 BHCs (the top group) and six bright candidate NS LMXBs (the bottom group) in observation 13820, for guidance regarding its form and content. Columns: (1) master source unique index; (2) observation ID; (3–5) the net counts in the broad band (0.5-7.0 keV) and the lower and upper limits; and (6-8) the energy flux in the broad band and the lower and upper limits in units of erg s⁻¹ cm⁻². All limits are at the 68% confidence level.

(This table is available in its entirety in machine-readable form.)

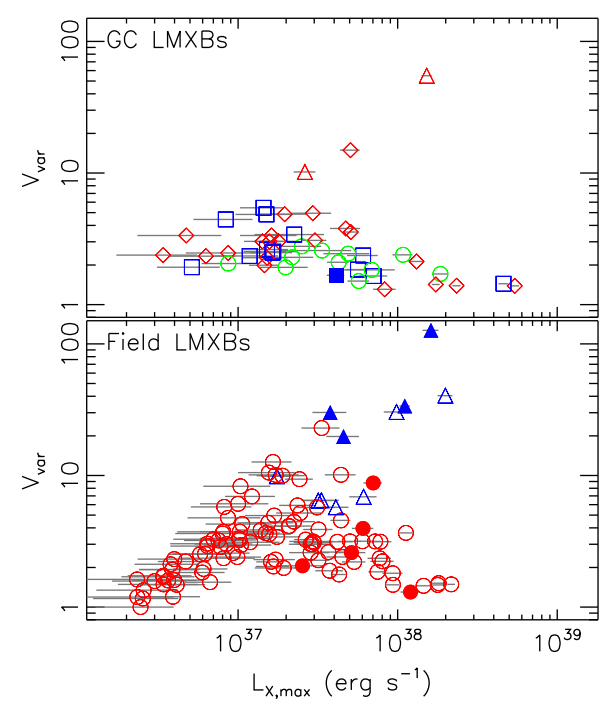


Figure 2. Long-term variability vs. the maximum 0.5–7 keV luminosity for all LMXBs, excluding those in the central a=10'' ellipse. The top panel is for GC LMXBs, with the blue squares and red diamonds for the HST/ACS blue/metal-poor and red/metal-rich GCs from Jennings et al. (2014), respectively, and the green circles for other GCs (the Subaru/Suprime-Cam GCs and the extra five HST/ACS GC candidates identified by us; Section 2.4). Two transients, both in red GCs, are plotted with red triangles. The bottom panel is for field LMXBs. The blue triangles denote the transient candidates. In both panels, the filled symbols denote BHCs (see the text for details).

compact objects of several masses ($M=1.4~M_{\odot}$, 3 M_{\odot} , 5 M_{\odot} , 10 M_{\odot} , and 20 M_{\odot}). We used the empirical relation between the real inner disk radius $r_{\rm in}$ and the normalization of the MCD model $N_{\rm MCD}$ (Kubota et al. 1998; Makishima et al. 2000):

$$r_{\rm in} = 1.19 \sqrt{\frac{N_{\rm MCD} d_{\rm 10kpc}^2}{\cos \theta}} \tag{2}$$

where $d_{10\mathrm{kpc}}$ is the source distance in units of 10 kpc and θ is the inclination angle. The relation takes into account the spectral hardening effect, with the hardening factor assumed to be 1.7, and the fact that the disk temperature does not peak at the inner radius. The dotted reference lines in Figure 6 assume $\theta=60^\circ$.

Here we focus on field LMXBs first, and present GC LMXBs in the next section. The most striking result of the PL fits to field LMXBs is the strong dependence of the photon index on the luminosity, as shown in the top middle panel in Figure 5. Most sources fall on a narrow track (the light gray region), with Γ_{PL} decreasing (thus the sources becoming harder) with increasing $L_{\rm X}$ up to $L_{\rm X}\sim7\times10^{37}\,{\rm erg\,s^{-1}}$ and then remaining at a value around 1.5 above this luminosity. Such a trend was indicated, although with larger scatters, in the luminosity versus hardness diagram in Figure 4. A few very soft outliers lying to the right of the light gray track can also be seen. Five of them are persistent sources (filled circles), and the other four are transients (filled triangles; S198 has two data points, corresponding to its high and low states). At $L_{\rm X}\lesssim2\times10^{37}\,{\rm erg\,s^{-1}}$, some hard sources with $\Gamma_{\rm PL}\lesssim1.8$ are

also present. We note that the lack of hard sources with $\Gamma_{PL} \lesssim 1.8$ at $L_X \lesssim 3 \times 10^{36} \, \mathrm{erg \, s^{-1}}$ is due to selection bias because we only fitted sources above 4σ , and harder sources tend to have lower significance levels at a given luminosity. The column density was inferred to be $\lesssim 0.4 \times 10^{22} \, \mathrm{cm^{-2}}$ for most sources. It seems to increase with the photon index, which could be caused by the use of a (non-physical) PL model to fit the spectra that are mainly thermal and are softer at lower luminosity (more discussion on the column density is given at the end of the section).

The MCD fits give results that are consistent with the PL fits. Most sources reside in the light gray region below the M=3 M_{\odot} dotted reference line (thus corresponding to lower mass) in the top middle panel plotting $L_{\rm X}$ versus $kT_{\rm MCD}$ in Figure 6, with $kT_{\rm MCD}$ increasing with $L_{\rm X}$ below $\sim 7 \times 10^{37}\,{\rm erg\,s^{-1}}$ and then remaining at around 1.5 keV above this luminosity. The very soft outliers identified from the PL fits fall in the region corresponding to $M\gtrsim 5\,M_{\odot}$. The column density of most sources from the MCD fits is at the minimum value allowed in the fits (i.e., the Galactic value).

To shed light on the possible nature of the sources, in the right panels of Figures 5 and 6, we plot the expected singlecomponent (PL and MCD) fitting results of three representative Galactic X-ray binaries—the atoll source 4U 1705–44 (filled red diamonds), the Z source GX 17+2 (green crosses), and the BHC XTE J1817-330 (filled blue squares)—based on the spectral fits of these sources by Lin et al. (2010, 2012a) and Rykoff et al. (2007), respectively. We assume them to be at the distance of NGC 3115 with absorption at the Galactic value in the direction of NGC 3115 (i.e., assuming zero intrinsic absorption). One reason to compare these sources with our sample is that they had high-quality broadband spectra spanning large luminosity ranges and were carefully modeled in the above studies. The spectra of 4U 1705–44 studied by Lin et al. (2010) used broadband observations by Suzaku (1.2-40 keV) and BeppoSAX (1-150 keV), and included two hard-state spectra and seven soft-state spectra over a large dynamical range (\sim 0.04–0.28 $L_{\rm Edd}$). For GX 17+2 , Lin et al. (2012a) compiled spectra over the whole Z track in the HID and used RXTE data ($\sim 3-40 \text{ keV}$), although for clarity we only used spectra at four critical positions: the two vertices and the two ends of the Z track in the HID. We selected XTE J1817–330 studied by Rykoff et al. (2007) to represent the spectral properties of BHBs because the outburst in their study was covered by Swift/XRT in the soft X-ray energy band of 0.5-10 keV, close to the *Chandra* bandpass, and spanned a large dynamical range, while the source is also one of the Galactic BHCs with the lowest absorption ($N_{\rm H} = 6 \times 10^{20}$ cm⁻²). Several spectral models were applied to these three sources in the above three studies, but we used the fits of the models that carefully addressed Comptonization (i.e., the SIMPL(MCD)+BB model, the MCD+BB+nthcomp model, and the MCD+comptt model in Lin et al. (2010, 2012a) and Rykoff et al. (2007), respectively). This is important because Comptonization with a steep slope can significantly overestimate the low-energy emission if it is fitted with models like a simple PL.

To convert the source flux to that at the distance of NGC 3115, we adopted the source distance of $d=7.4\,\mathrm{kpc}$ for 4U 1705–44 (Haberl & Titarchuk 1995), $d=8.1\,\mathrm{kpc}$ for GX 17+2 (Lin et al. 2012a), and $d=10\,\mathrm{kpc}$ for XTE J1817–330 (as assumed in Rykoff et al. 2007). The distance of 4U 1705–44

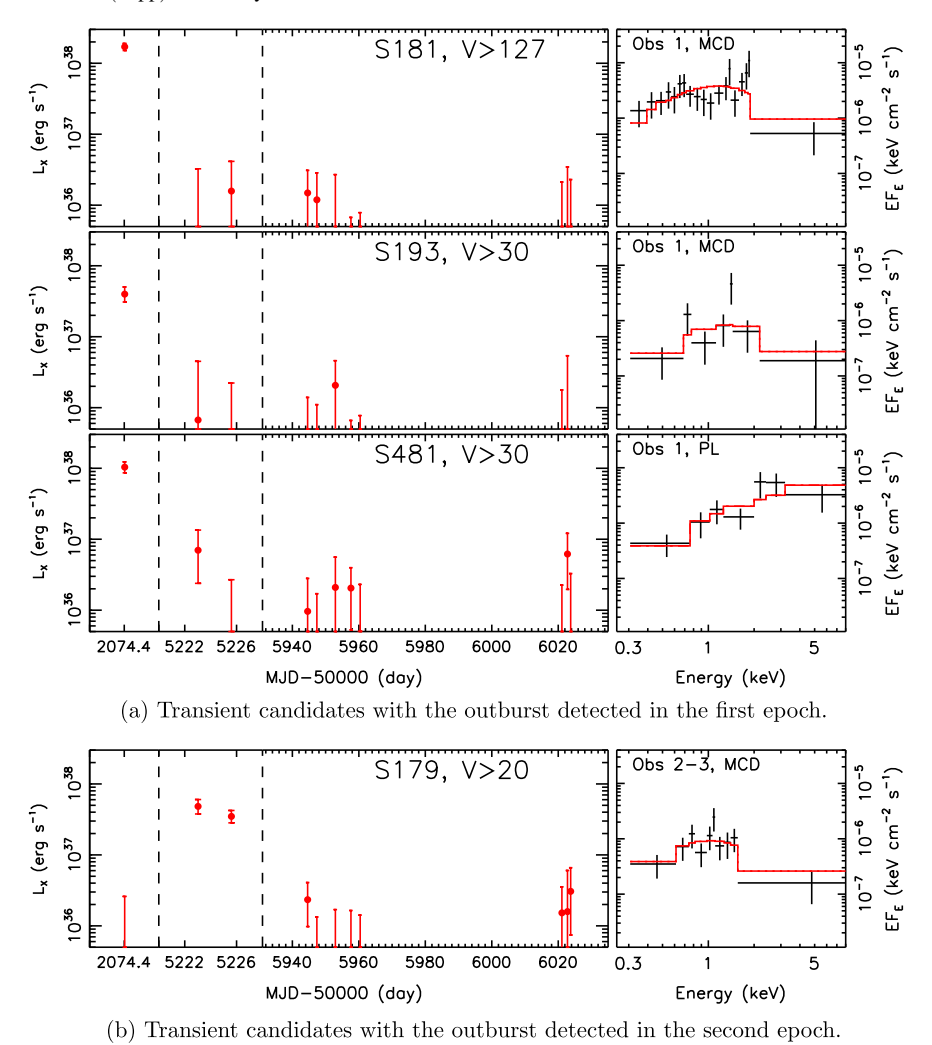


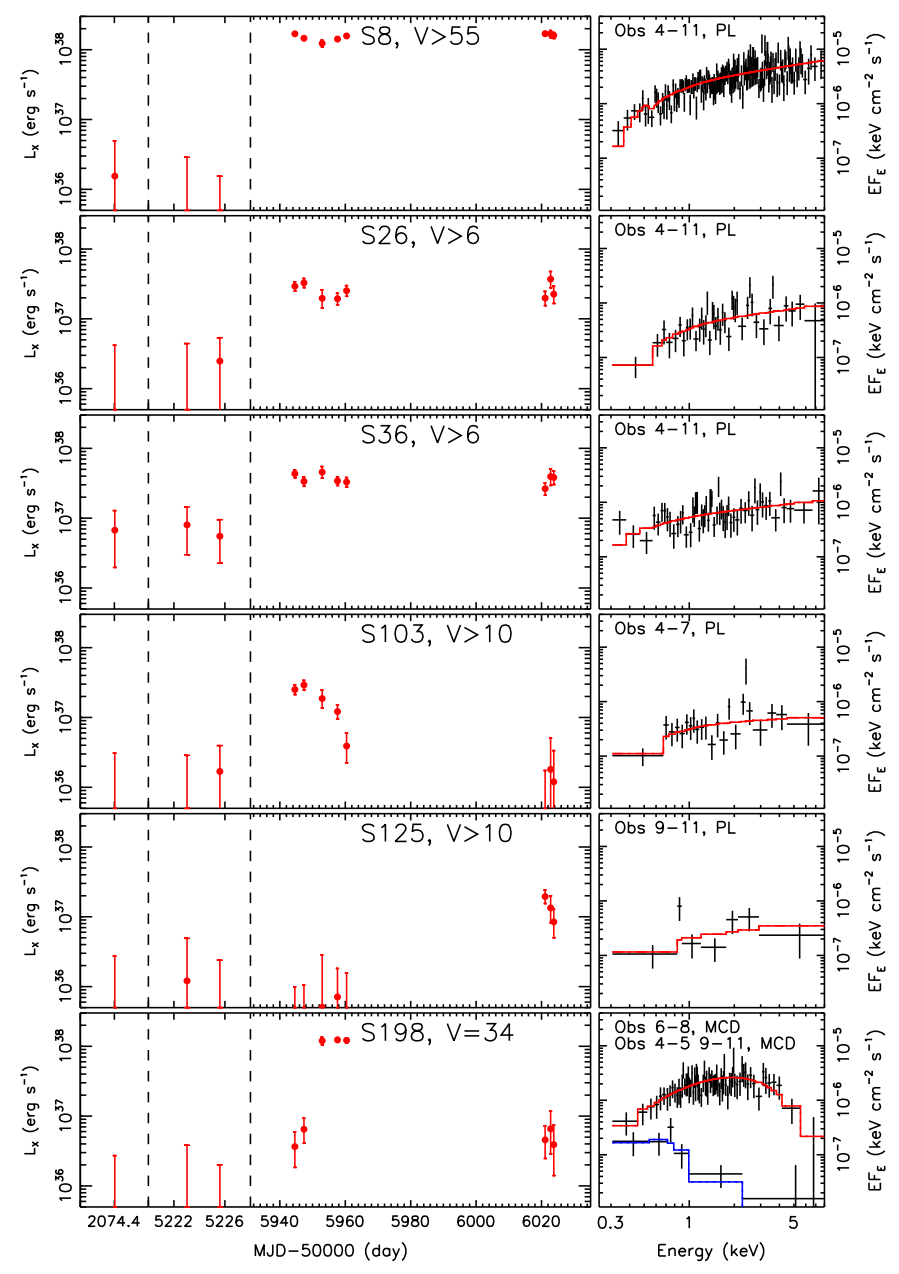
Figure 3. Long-term light curve (left panels, with the source number and long-term variability V (i.e., V_{var} in Section 2.3)) and sample spectra (right panels, with annotations for the observations and spectral models used) for special sources.

was derived from type I X-ray bursts and has a relatively small uncertainty (\sim 20%) depending on the abundance of the accreted material assumed (Galloway et al. 2008). The distance of GX 17+2 was also derived based on type I X-ray bursts, but the bursts in this source exhibited abnormal properties, which could lead to a relatively large uncertainty (\sim 50%) on the distance derived (Lin et al. 2012a). There is no reliable distance estimate for XTE J1817–330. The distance of 10 kpc implied a BH of 10 M_{\odot} , based on Equation (2); (Rykoff et al. 2007). As long as the central BH is not too small and the Eddington ratio of the thermal state in this source is not too low (\gtrsim 1%), we expect its distance to be close to 10 kpc (within a factor of two). The above distance uncertainties of GX 17+2 and XTE J1817–330 are small enough and do not significantly affect our comparison of these sources with the sources in NGC 3115.

For each spectrum of the representative Galactic X-ray binaries, we generated 200 simulations and fitted them with PL and MCD models. The data plotted in Figures 5 and 6 are the median of the fitting results, with the error bars representing the intervals including 90% of the fits. In the PL and MCD fits to the simulated 0.3–8 keV spectra of the seven soft-state observations of 4U 1705–44, we inferred the photon index to decrease from 1.9 to 1.3 (the top right panel in Figure 5) or the disk temperature to increase from 1.1 to 2.1 keV (the top right

panel in Figure 6) as the 0.3–8 keV luminosity increases from 10^{37} to 7×10^{37} erg s⁻¹. Such trends are very similar to those traced out by a majority of our field LMXBs in the light gray region in Figures 5 and 6 in a similar luminosity range. GX 17 +2 shows similarly hard spectra to the brightest observation of 4U 1705–44 in 0.3–8 keV, with $\Gamma_{\rm PL} \sim 1.4$ from the PL fits and $kT_{\rm MCD} \sim 2$ keV from the MCD fits. Such properties are similar to those of the brightest field sources.

Based on this comparison, we suggest that the light gray region in Figures 5 and 6 marks an NS LMXB soft-state track, with sources below $L_{\rm X} \sim 7 \times 10^{37} \, {\rm erg \, s^{-1}}$ being atolls in the soft state and brighter sources being Z sources. Thus the observation that most of our sources appear harder at higher luminosity in 0.3-8 keV can be easily explained because for the atoll soft state, the temperatures of the disk and boundary layer thermal emission increase with luminosity at relatively constant emission areas (Lin et al. 2007, 2009, 2010). Such trends are not seen in Z sources because the inner disk and the boundary layer reach the local Eddington limit, in which case the change in the accretion rate tends to lead to change in the emission area (the inner radius for the disk), instead of the temperature (Lin et al. 2009). We note that our sources seem systematically slightly softer than the simulated spectra of Galactic NS LMXBs, and one explanation for this is the possible presence



(c) Transient candidates with the outburst detected in the third epoch.

Figure 3. (Continued.)

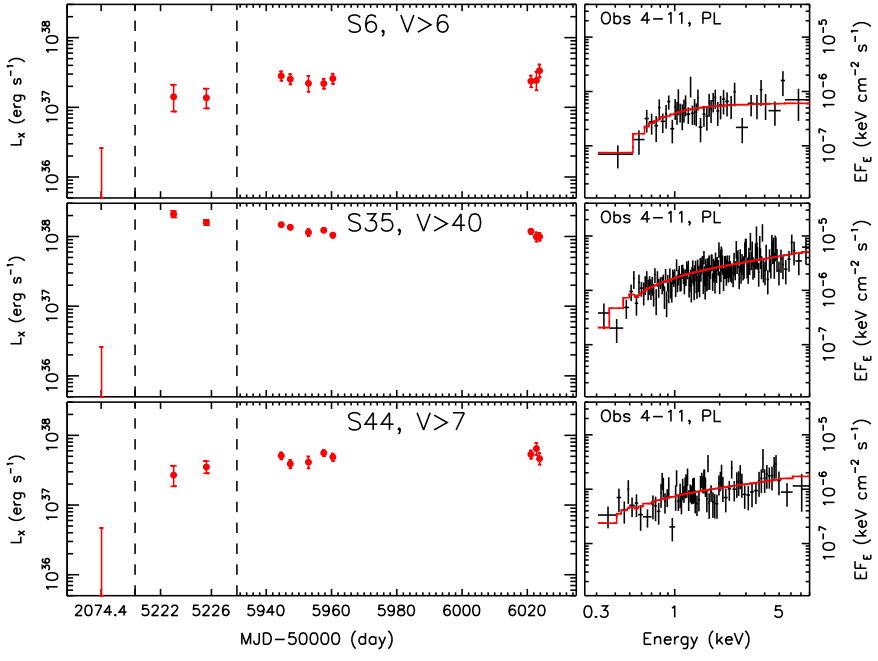
of soft excess of the real disk spectrum compared with the simple MCD description (i.e., *diskbb* in XSPEC) used in Lin et al. (2010) and Lin et al. (2012a), which will be discussed in Section 4.2.

Although the soft-state observations of 4U 1705–44 in Lin et al. (2010) are above $L_{\rm X}\sim 10^{37}\,{\rm erg~s}^{-1}$, atolls in the soft state can be fainter. For example, the soft state of 4U 1608–52 has Eddington ratios as low as 0.01 (Lin et al. 2007), which is four times lower than 4U 1705–44 in Lin et al. (2010). Therefore, the atoll soft-state explanation could apply to our relatively soft ($\Gamma_{\rm PL}\gtrsim 2.0$) faint sources with $L_{\rm X}$ as low as a few $10^{36}\,{\rm erg~s}^{-1}$.

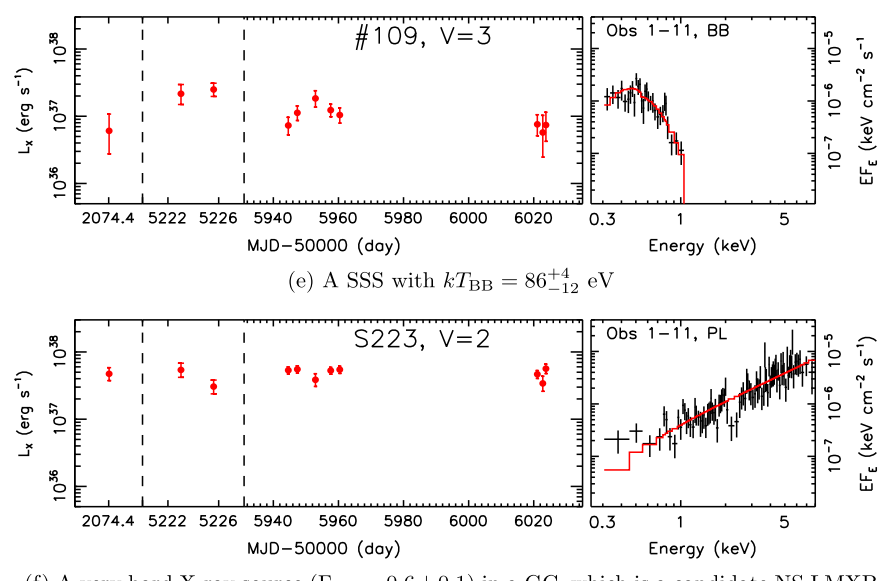
As mentioned, we also have nine very soft outliers (filled circles and triangles in the middle panels in Figures 5 and 6). They are much softer than NS LMXBs at corresponding luminosities, but are similar to the BHC XTE J1817–330 in the

thermal state. Therefore, we identified them as BHCs. Their long-term luminosity curves and sample spectra are shown in Figure 3 (those fitted with an MCD or MCD+PL model), and the PL and MCD fit results are given in Table 6. The spectra of most of these BHCs can be described with an MCD, except S100. This source seems to show a hard tail, and we tried to fit it with an MCD plus a PL, with the photon index fixed at a value of 2.5. The fitting result is included in Table 7, indicating the presence of a PL at the 6σ confidence level. S198 is an interesting BHC that will be described separately in Section 3.4.1. It is the only source with two spectra (one in the high state and the other in the low state, Section 3.4.1, Figure 3(c)) in Figures 5 and 6.

The faint hard sources with $L_{\rm X} \lesssim 2 \times 10^{37}\,{\rm erg\,s^{-1}}$ and $\Gamma_{\rm PL} \lesssim 1.8$ could be atolls in the hard state, similar to the two



(d) Transient candidates with the outburst detected in the second and third epochs.



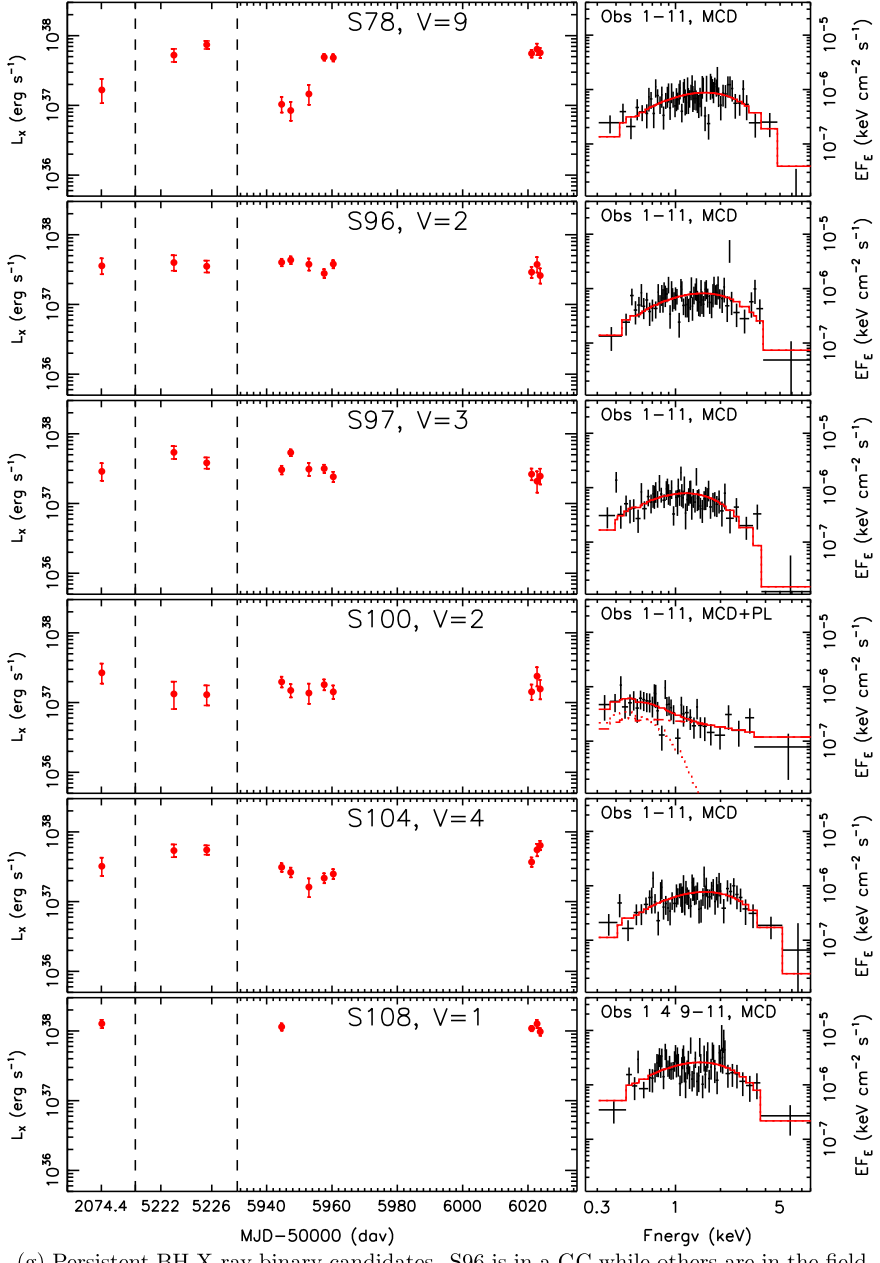
(f) A very hard X-ray source ($\Gamma_{\rm PL}=0.6\pm0.1$) in a GC, which is a candidate NS LMXB with a strong magnetic field or a high inclination.

Figure 3. (Continued.)

hard-state spectra of 4U 1705–44 (the two filled diamonds below 8 \times 10³⁶ erg s⁻¹ in Figures 5 and 6). We cannot rule out the possibility that there may be some BHBs in the hard state. For example, simulating the hard-state spectrum of the BHB GX 339–4 studied by Miller et al. (2006) and fitting with a PL, as we did for other three Galactic X-ray binaries, gave $L_{\rm X} \sim 2 \times 10^{37} \, {\rm erg \ s^{-1}}$ and $\Gamma_{\rm PL} \sim 1.6$. However, considering that NS LMXBs are expected to be more common than BHBs, the possibility of being BHBs should be low.

Our PL fits to the simulated spectra of three Galactic X-ray binaries in the soft/thermal state systematically gave column densities larger than the value assumed in the simulation

(i.e., the Galactic value toward NGC 3115; see the bottom right panel in Figure 5). Therefore, the column densities from the PL fits to our sources are systematically overestimated if the identification of our sources is correct (i.e., most sources are NS LMXBs in the soft state with the very soft outliers being BHBs in the thermal state). On the other hand, the MCD fits tend to underestimate the column density, due to the presence of a hard component (weak Comptonization in the case of BHBs in the thermal state or the boundary layer emission in the case of NS LMXBs in the soft state) and/or possible extra soft emission of the real disk spectrum relative to the MCD description, which will be discussed in Section 4.



(g) Persistent BH X-ray binary candidates. S96 is in a GC while others are in the field. S108 has only five detections because it is in the CCD gap in other observations.

Figure 3. (Continued.)

There is one main caveat of comparing our sources with Galactic sources. To have enough statistics, we used spectra of our sources that were accumulated over long exposures (\sim 1.1 Ms) and spanning more than a decade, although most data were made from the XVP, which still covered nearly three months. To reduce this problem, we carefully created spectra for transients by combining only observations with similar fluxes. For the other sources, if $L_{\rm X, max} \gtrsim 2 \times 10^{37} \, {\rm erg \, s^{-1}}$, most have a long-term variability $V_{\rm var} \lesssim 3$, which is not large enough to significantly affect our comparison with Galactic sources. However, for fainter sources, their long-term variability is uncertain, and there might be relatively large systematic errors produced by the dependence of the spectral properties on the luminosity obtained.

3.3.3. Spectral Fits of GC LMXBs

On the whole, the simple PL and MCD fits indicate that GC LMXBs have spectral properties that are very similar to those of field LMXBs (compare the left panels for GC LMXBs and the right panels for field LMXBs in Figures 5 and 6). In particular, most GC sources are also in the NS LMXB soft-state track (the light gray region), which exhibits a trend of decreasing $\Gamma_{\rm PL}$ or increasing $kT_{\rm MCD}$ with an increase in $L_{\rm X}$ below $L_{\rm X}\sim 7\times 10^{37}\,{\rm erg\,s^{-1}}$ and relatively constant $\Gamma_{\rm PL}$ (~1.5) or $kT_{\rm MCD}$ (~1.5 keV) above this luminosity. As discussed in the previous section for field LMXBs, most of our GC LMXBs below and above $L_{\rm X}\sim 7\times 10^{37}\,{\rm erg\,s^{-1}}$ in this track could be atolls in the soft state and Z sources, respectively. Some hard sources with $\Gamma<1.8$ below

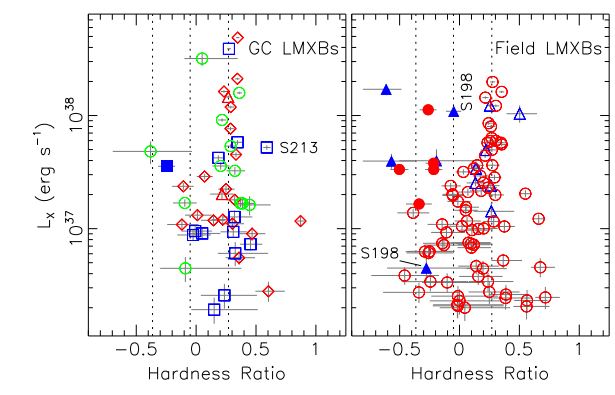


Figure 4. 0.5–7 keV luminosity vs. the hardness ratio for candidate LMXBs above 4σ (excluding those in the central a=10'' ellipse). The hardness ratio is defined as HR = (H - S)/(H + S), where S and H are the energy fluxes in the 0.5-2 keV and 2-7 keV energy bands, respectively. The luminosities and hardness ratios were calculated from the merged observation, except for the 13 transients, for which the merged high-state and low-state observations (Figures 3 (a)-(d)) were used. The left panel is for GC LMXBs, with the blue squares and red diamonds for the HST/ACS blue/metal-poor and red/ metal-rich GCs from Jennings et al. (2014), respectively, and the green circles for other GCs (the Subaru/Suprime-Cam GCs and the extra five HST/ACS GC candidates identified by us; Section 2.4). Two transients, both in red GCs, are plotted with red triangles. The filled square marks the BHC S96. The right panel is for field LMXBs. The blue triangles denote the transient candidates. The filled circles and triangles denote the BHCs. The error bars in both panels are at the 1σ confidence level. The vertical dotted lines from right to left in both panels correspond to hardness ratios for an unabsorbed PL with Γ = 1.5, 2.0, and 2.5, respectively.

 $L_{\rm X}\sim 3\times 10^{37}\,{\rm erg\,s^{-1}}$ are also present, and they could be NS or BH LMXBs in the hard state. It seems that GC LMXBs have more hard sources at luminosities around $10^{37}\,{\rm erg\,s^{-1}}$ than field LMXBs. For example, over the range $L_{\rm X}=(1\text{--}2)\times 10^{37}\,{\rm erg\,s^{-1}}$, six out of 10 GC LMXBs have $\Gamma<1.6$, but only one out of 14 field LMXBs have $\Gamma<1.6$, from the PL fits.

There is one persistent source, S96, in a blue/metal-poor GC (the filled square in the left panels in Figures 5 and 6) whose spectrum is significantly softer than those of other sources at similar luminosity ($L_{\rm X}\sim3\times10^{37}~{\rm erg~s^{-1}}$). Its long-term luminosity curve and merged spectrum are shown in Figure 3(g). We identified it as a BHC. There is another source, S223, which is much harder than other sources at similar luminosity ($L_{\rm X}\sim10^{38}~{\rm erg~s^{-1}}$); it is a candidate NS LMXB with a high magnetic field or a high inclination and will be presented separately in Section 3.4.3.

3.3.4. CXB Sources

The results of PL fits to CXB sources are shown in Figure 7. Sources inside and outside $2D_{25}$ are plotted in the left and right panels, respectively. For both groups of sources, we see no clear dependence of the photon index on the flux and column density. By using sources outside $2D_{25}$, excluding extreme sources with $\Gamma_{\rm PL} > 3.5$ and those with $\Gamma_{\rm PL} < 0.5$, and limiting to $L_{\rm X} > 2 \times 10^{-15}\,{\rm erg\,s^{-1}\,cm^{-2}}$, we obtained a median of $\Gamma_{\rm PL} = 1.77$ with 68.3% within 0.38 around it, which is consistent with the results from Lin et al. (2012b).

In Figure 7, we include three sources (triangles; S317, S362, and S372) that are candidate coronally active stars because they all have $\Gamma_{PL} >$ 3.5, coincide with bright stars in the Subaru/

Suprime-Cam imaging, and have possible stellar flares detected, as shown in the bottom three panels in Figure 8. Two faint soft sources ($\Gamma_{PL} \gtrsim 2.6$; S288 and S290) are plotted with squares. Since they are coincident with bright extended galaxies in the Subaru/Suprime-Cam imaging, they might be due to hot gas emission in the galaxies.

3.4. Special Sources

3.4.1. S198: A Transient BH LMXB Candidate with a Prominent Disk at a Very Low State

As shown in Section 3.2, S198 is the only source whose outburst is covered relatively well by our observations (Figure 3(c)). It also has the most clear spectral evolution caught among our sources. To accumulate enough statistics, we combined all the data in the rising (observations 4-5) and decay (observations 9-11) stages to create a low-state spectrum (the spectra in these two stages seem to be consistently soft) and the others (6-8) for a high-state spectrum. When we adopted the PL model, we obtained $\Gamma_{PL}=2.6\pm0.3$ for the high state and $\Gamma_{PL} > 4.2$ (the 90% lower limit) for the low state (the absorption for the low state was fixed at the value obtained from the fit to the high state; Table 6). Using the MCD model, we obtained $kT_{\rm MCD} = 0.78 \pm 0.07 \, {\rm keV}$ for the high state and $kT_{\rm MCD} = 0.17 \pm 0.05 \, {\rm keV}$ for the low state. Therefore, the spectrum of S198 in the low state in the 2012 outburst is much softer than in the high state. The $0.3-8 \text{ keV } L_X$ is about 0.12and 0.008 Eddington luminosity (assuming a BH of mass $M_{\rm BH}=6~M_{\odot}~({\rm see~below})$ and a disk inclination of $60^{\circ})$ in the high and low states, respectively.

The disk temperature and luminosity in the high state are typical for BHBs in the thermal state (Figure 6; also refer to Figure 16 in Done et al. 2007), in which the thermal disk emission dominates (Remillard & McClintock 2006). Based on Equation (2) and the MCD fit in Table 6 and assuming a disk inclination of 60° , the BH has a mass about $6 M_{\odot}$.

The low state is more difficult to understand, so to determine the corresponding spectral state, we compare our source with Swift J1753.5–0127 in Rykoff et al. (2007). We first checked for the possible presence of a PL component in the low state by adding a PL to the MCD model in the fit to the spectrum. We fixed $\Gamma_{PL}=1.7$ and $\Gamma_{PL}=2.5$, which are typical values seen in BHBs, and found that the PL component contributes less than 23% and 37% (90% upper limit) of the 0.3–8 keV unabsorbed flux, respectively. Thus the MCD still dominates in this energy range in such fits. In comparison, Swift J1753.5-0127 has a disk thermal flux fraction of about 71%, 62%, and 56% in observations 15, 16, and 17 (those with $L_{\rm X} \sim 1.4 \times 10^{37}$ erg s⁻¹, 2.5×10^{37} erg s⁻¹, and 3.4×10^{37} erg s⁻¹ in Figures 5 and 6) in Rykoff et al. (2007), respectively. The disk temperatures are about 0.19, 0.25, and 0.33 keV, and the Eddington ratios are about 0.010, 0.019, and 0.026 (assuming a BH mass of 10 M_{\odot} and a source distance of 10 kpc) in these three observations, respectively (Rykoff et al. 2007). The source was probably in the transitional state in observations 15 and 16 and in the hard state in observation 17, based on the broadband data from the Proportional Counter Array onboard the RXTE (Gierliński et al. 2008). While Rykoff et al. (2007) concluded that the inner disk radius was consistent with the ISCO in all the three and other brighter Swift observations, Gierliński et al. (2008) demonstrated that the inner disk receded from the ISCO in observations 15–17, after taking into

Table 6
Spectral Fit Results

			The PL	Model			The M	ICD Model	
Source	Obs	$N_{ m H}$	Γ	Norm	L	$N_{ m H}$	kT	R	L
(1)	(2)	(3)	(4)	(5)	(6)	(7)	(8)	(9)	(10)
78	0	$18.0^{+8.4}_{-7.2}$	$2.84^{+0.35}_{-0.32}$	$1.31^{+0.39}_{-0.28}$	$3.1^{+0.5}_{-0.3}$	$0.0^{+2.1}$	$0.64^{+0.07}_{-0.06}$	39.09 ^{+8.86} _{-7.64}	$3.0^{+0.3}_{-0.3}$
96	0	$14.4^{+7.6}_{-7.1}$	$2.79_{-0.33}^{+0.35}$	$1.12^{+0.32}_{-0.24}$	$3.0^{+0.4}_{-0.4}$	$0.0^{+1.4}$	$0.62^{+0.07}_{-0.06}$	$40.65^{+9.85}_{-8.07}$	$2.8^{+0.3}_{-0.4}$
97	0	$16.7^{+9.0}_{-7.6}$	$3.36^{+0.45}_{-0.41}$	$1.25^{+0.42}_{-0.30}$	$2.8^{+0.4}_{-0.4}$	$0.0^{+1.4}$	$0.45^{+0.05}_{-0.04}$	$76.14^{+18.28}_{-15.39}$	$2.6^{+0.3}_{-0.2}$
100	0	$0.0^{+3.5}$	$3.08^{+0.30}_{-0.24}$	$0.38^{+0.06}_{-0.04}$	$2.3_{-0.4}^{+0.3}$	$0.0^{+1.0}$	$0.29^{+0.05}_{-0.04}$	$152.16^{+60.41}_{-49.81}$	$1.5^{+0.3}_{-0.2}$
104	0	$16.5^{+8.5}_{-7.5}$	$2.76^{+0.37}_{-0.34}$	$1.09^{+0.34}_{-0.25}$	$2.8^{+0.4}_{-0.4}$	$0.0^{+2.3}$	$0.64^{+0.08}_{-0.07}$	$36.70_{-7.36}^{+9.34}$	$2.6^{+0.2}_{-0.2}$
108	0	$24.9^{+8.8}_{-8.2}$	$3.24^{+0.40}_{-0.37}$	$4.95^{+1.59}_{-1.14}$	$8.7^{+1.1}_{-0.9}$	$0.0^{+3.9}$	$0.59^{+0.07}_{-0.07}$	$79.87^{+24.27}_{-13.20}$	$8.7^{+0.8}_{-1.1}$
179	h	$31.1^{+26.5}_{-26.1}$	$4.21^{+0.79}_{-1.44}$	$2.26^{+2.77}_{-1.33}$	$2.8^{+1.3}_{-0.8}$	$0.0^{+20.1}$	$0.39^{+0.13}_{-0.14}$	$111.52^{+279.70}_{-51.07}$	$3.0^{+0.8}_{-0.9}$
181	h	$10.1^{+13.0}_{-10.1}$	$2.96^{+0.84}_{-0.69}$	$4.58^{+2.88}_{-1.61}$	$14.0^{+4.0}_{-3.1}$	$0.0^{+3.5}$	$0.45^{+0.11}_{-0.08}$	$171.01^{+92.25}_{-59.61}$	$12.4^{+2.5}_{-2.1}$
193	h	$9.0^{+77.7}_{-9.0}$	$2.46^{+2.54}_{-1.03}$	$0.94^{+8.05}_{-0.49}$	$3.3^{+2.7}_{-1.8}$	$0.0^{+31.0}$	$0.57^{+0.43}_{-0.25}$	$49.15^{+201.12}_{-31.44}$	$2.8^{+1.5}_{-1.1}$
198	h	$20.3^{+9.4}_{-8.3}$	$2.59^{+0.34}_{-0.32}$	$3.63^{+1.12}_{-0.84}$	$9.3^{+1.4}_{-1.2}$	$0.0^{+3.5}$	$0.80^{+0.10}_{-0.09}$	$43.19^{+11.46}_{-8.68}$	$9.0^{+0.9}_{-1.2}$
198	1	20.3(f)	$5.00_{-0.80}$	$0.18^{+0.08}_{-0.06}$	$0.5^{+0.2}_{-0.2}$	0.0(f)	$0.17^{+0.07}_{-0.04}$	$345.30^{+481.98}_{-235.01}$	$0.6^{+0.4}_{-0.2}$
8	h	$5.9^{+4.2}_{-4.1}$	$1.57^{+0.13}_{-0.13}$	$2.57^{+0.36}_{-0.32}$	$18.0^{+1.7}_{-1.2}$	$0.0^{+0.6}$	$1.47^{+0.13}_{-0.11}$	$17.12^{+2.52}_{-2.28}$	$16.2^{+1.6}_{-1.4}$
25	0	$3.2^{+3.5}_{-3.2}$	$1.43^{+0.11}_{-0.11}$	$2.54^{+0.29}_{-0.27}$	$21.3_{-1.4}^{+1.5}$	$0.0^{+0.6}$	$1.62^{+0.14}_{-0.10}$	$15.31^{+2.00}_{-1.92}$	$18.9^{+1.8}_{-1.7}$
35	h	$3.6^{+4.3}_{-3.6}$	$1.54^{+0.14}_{-0.14}$	$2.03^{+0.31}_{-0.27}$	$15.1^{+1.5}_{-1.3}$	$0.0^{+0.6}$	$1.45^{+0.14}_{-0.12}$	$15.91^{+2.70}_{-2.40}$	$13.4^{+1.3}_{-1.2}$
68	0	$1.5^{+3.0}_{-1.5}$	$1.48^{+0.10}_{-0.09}$	$3.10^{+0.33}_{-0.27}$	$25.2_{-1.7}^{+1.8}$	$0.0^{+0.4}$	$1.51^{+0.11}_{-0.10}$	$19.08^{+2.42}_{-2.32}$	$22.2^{+2.1}_{-1.0}$
200	0	$5.7^{+2.4}_{-2.2}$	$1.46^{+0.07}_{-0.07}$	$8.14^{+0.59}_{-0.55}$	$63.7^{+3.0}_{-2.9}$	$0.0^{+0.4}$	$1.61^{+0.08}_{-0.02}$	$27.02^{+0.54}_{-0.55}$	$57.0^{+2.7}_{-2.6}$
212	0	$9.3^{+3.7}_{-3.6}$	$1.62^{+0.09}_{-0.09}$	$7.09^{+0.74}_{-0.61}$	$45.4^{+2.1}_{-2.0}$	$0.0^{+0.6}$	$1.53^{+0.09}_{-0.02}$	$25.54^{+0.51}_{-0.52}$	$42.1^{+2.0}_{-1.9}$

Note. A portion is shown here, using 10 BHCs (the top group) and six bright candidate NS LMXBs (the bottom group), for guidance regarding its form and content. Columns: (1) master source unique index; (2) the observation ("0" refers the combination of all available observations; "h" refers to the combination of the high-state observations for the 13 transients, as shown in Figures 3(a)–(d); and "l" refers to the combination of the low-state observations for source 198, as shown in Figure 3(c)); (3)–(6) the intrinsic column density (in units of 10^{20} cm⁻², constrained to be $\leq 10^{23}$ cm⁻²), photon index (constrained to be ≤ 5.0), normalization (in units of 10^{-6} photons keV⁻¹ cm⁻² s⁻¹ at 1 keV), and 0.3–8 keV luminosity (in units of 10^{37} erg s⁻¹, assuming a source distance of 9.7 Mpc) corrected for Galactic absorption from the fit with the PL model; (7)–(10) the intrinsic column density, the maximum disk temperature (in units of keV, constrained to be ≤ 4 keV), the apparent inner disk radius R_{MCD} (in units of km) from the normalization $N_{\text{MCD}} \equiv ((R_{\text{MCD}}/\text{km})/(D/10 \text{ kpc}))^2 \cos \theta$ (where D is the source distance 9.7 Mpc and θ is the disk inclination assumed to be 60°), and 0.3–8 keV luminosity corrected for Galactic absorption from the fit with the MCD model. All fits used the C statistic. All errors are at the 90% confidence level. For S198, the fit to the low-state spectrum has the column density fixed (marked with "f") at the value obtained from the fit to the high-state spectrum.

(This table is available in its entirety in machine-readable form.)

account the effect of irradiation from the hot corona on the disk. The inner disk radius in the low state of S198 is about three times larger than that in the high/thermal state, although only at the 2.2σ level (Table 6). Therefore, based on the disk temperature, the Eddington ratio, and the larger inner disk radius than in the high state, in the low state S198 could be similar to Swift J1753.5–0127 in observation 17 (i.e., in the hard state). Alternatively and probably more likely, it could be in the transitional state, considering its more prominent disk than Swift J1753.5–0127 in observation 17.

3.4.2. S109: A SSS

SSSs have a characteristic temperature $\lesssim 0.1 \, \mathrm{keV}$ and have been seen in our Milky Way, the Magellanic Clouds, and nearby galaxies (for a recent review, see Di Stefano et al. 2010). S109 is the only SSS in our source sample. Its long-term light curve and sum spectrum are shown in Figure 3(e). The source seems persistent with $V_{\rm var} = 3$. The spectrum can be fitted with a BB with $kT_{\rm BB} = 86^{+4}_{-12} \, \mathrm{eV}$ and apparent emission radius $R_{\rm BB} = 3.4^{+5.3}_{-0.7} \times 10^3 \, \mathrm{km}$ (Table 7). The unabsorbed bolometric luminosity is $(0.8^{+2.2}_{-0.2}) \times 10^{38} \, \mathrm{erg \, s^{-1}}$. SSSs with luminosity around the Eddington limit for a white dwarf (WD; i.e., $\sim 10^{38} \, \mathrm{erg \, s^{-1}}$), could be nuclear

burning of material accreted by a WD (Greiner 2000). Therefore our SSS is probably one such source.

3.4.3. S223: A Very Hard Luminous X-Ray Source in a GC

As shown in Section 3.3.3, S223 has a spectrum that is significantly harder ($\Gamma_{PL}=0.6\pm0.1$) than other sources ($\Gamma_{PL}\gtrsim1.4$). The source seems persistent, with a long-term variability factor of $V_{var}=1.8$ at the 2.2σ significance level and a mean 0.3–8 keV luminosity of 0.96×10^{38} erg s⁻¹ (Figure 3(f)). We detected short-term variability in observation 11, with a Gregory–Loredo variability index of 6 (Figure 8), but not in other observations, with Gregory–Loredo variability index of ≤ 1 . The source is coincident with a spectroscopically confirmed GC, whose g-z color (1.1) is close to the boundary value of 1.13 used to separate the blue and red GCs (Paper III). Therefore it is very unlikely to be a background AGN or a foreground star. It is probably not composed of multiple sources in the same GC, considering the detection of both long-term and short-term variability.

Other X-ray sources were also found to show very hard spectra and high luminosities and reside in GCs in nearby galaxies. Burke et al. (2013) reported a source (their S48) in a GC in Centaurus A having $\Gamma_{PL} \sim 0.7$ and the 0.5–10 keV luminosity $\sim 6 \times 10^{37} \, \mathrm{erg \, s^{-1}}$. Trudolyubov & Priedhorsky

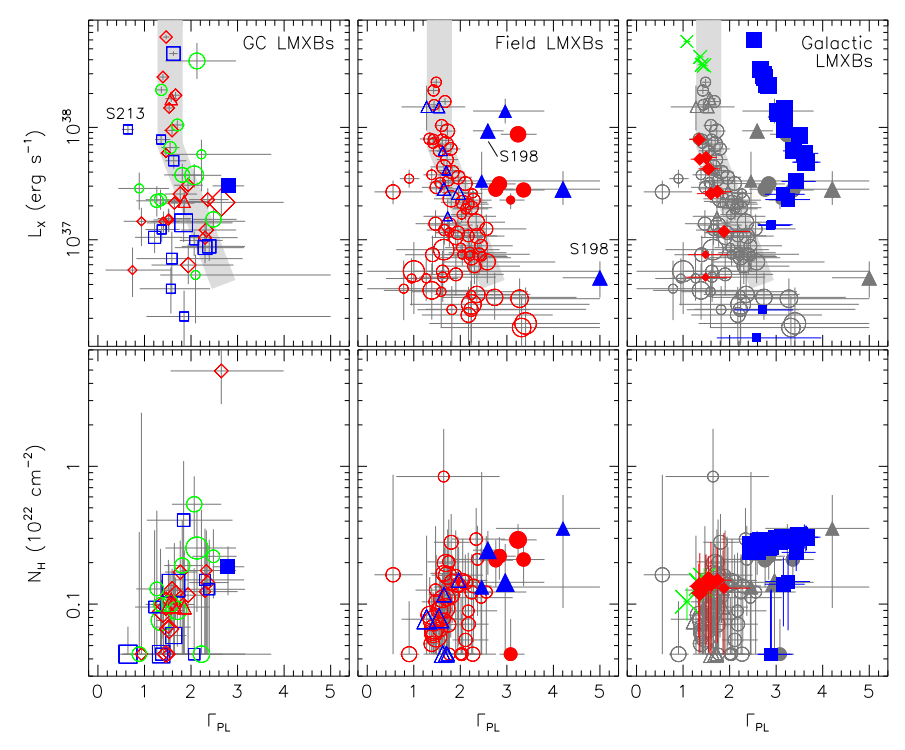


Figure 5. PL fit results of LMXBs, excluding those in the central a=10'' ellipse, with the top panels plotting the 0.3–8 keV luminosity vs. the photon index (symbol size proportional to column density logarithm) and the bottom panels plotting the column density (including the Galactic absorption) vs. the photon index (symbol size proportional to luminosity logarithm, using data with $L_X > 8 \times 10^{36}$ erg s⁻¹ for clarity). The left and middle panels are for GC and field LMXBs, respectively (the meanings of the symbols are the same as in Figure 4). The right panels plot the PL fits to the atoll source 4U 1705–44 (filled diamonds), the Z source GX 17+2 (crosses), and the BHC XTE J1817–330 (filled squares), based on the spectral fits of these sources by Lin et al. (2010), Lin et al. (2012a), and Rykoff et al. (2007), respectively, and assuming them to be at the distance of NGC 3115 with only Galactic absorption ($N_{\rm H} = 4.32 \times 10^{20}$ cm⁻²). In these panels we also plot the data shown in the middle panels for field LMXBs, but in a gray color. In all panels the error bars (sometimes smaller than the symbol size) correspond to the 90% confidence level. The light gray region in the top panels marks the possible NS LMXB soft-state track, where atolls in the soft state and Z sources reside.

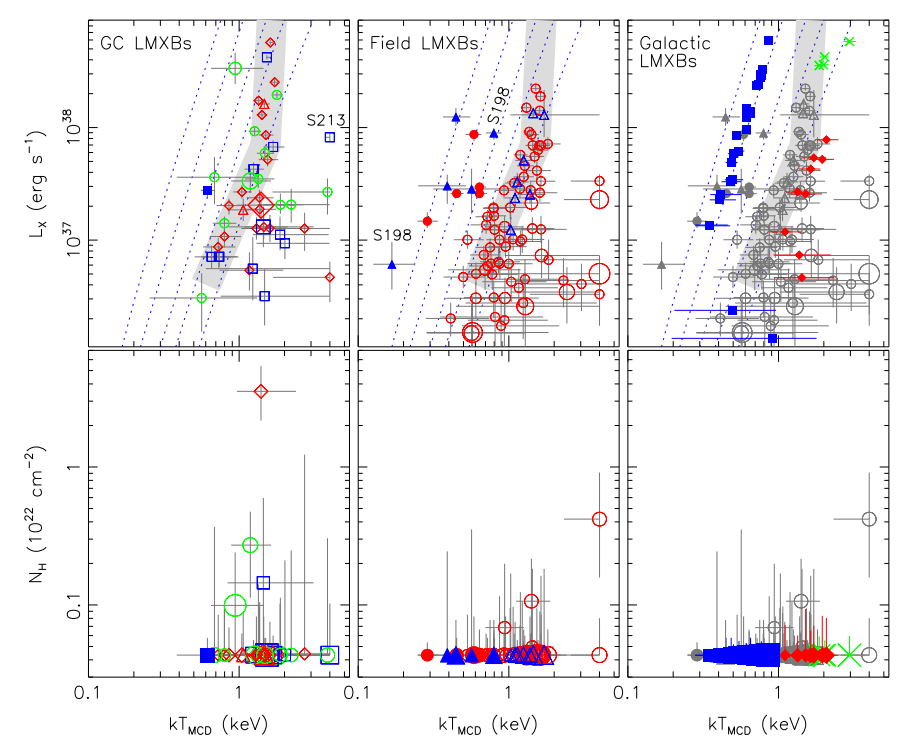


Figure 6. Similar to Figure 5 but for the MCD fits. The dotted lines in the upper panels show the expected dependence of the 0.3-8 keV luminosity $L_{\rm X}$ on $kT_{\rm MCD}$ from the standard thermal disk truncated at the ISCO of compact objects of several masses ($M=1.4~M_{\odot}$, $3~M_{\odot}$, $5~M_{\odot}$, $10~M_{\odot}$, and $20~M_{\odot}$) corresponding to lines from the right to the left, respectively; see the text for details. The light gray region in the top panels marks the possible NS LMXB soft-state track, where atolls in the soft state and Z sources reside.

Table 7Spectral Fit Results of Some Special Sources

Source	Model	$N_{ m H}$	Other Parameters	χ_{ν}^2/ν	$L_{ m abs}$	$L_{\rm unabs}$
		$(10^{20}\mathrm{cm}^{-2})$			$(10^{36} \epsilon$	$erg s^{-1}$
(1)	(2)	(3)	(4)	(5)	(6)	(7)
100	MCD+PL	0.0+7.2	$kT_{\text{MCD}} = 0.14^{+0.05}_{-0.04} \text{ keV}, R_{\text{MCD}} = 660^{+1463}_{-437} \text{ km}, \Gamma_{\text{PL}} = 2.5(f), N_{\text{PL}} = (0.26^{+0.07}_{-0.07}) \times 10^{-6}$	•••	22^{+4}_{-3}	22^{+15}_{-3}
109	ВВ	0.7 ^{+10.6}	$kT_{\rm BB} = 0.086^{+0.007}_{-0.012} \text{keV}, R_{\rm BB} = 3376^{+5272}_{-674} \text{km}$	•••	37 ⁺⁷ ₋₁₀	41^{+79}_{-8}
8	MCD+BB	0.0+3.2	$kT_{\text{MCD}} = 0.67_{-0.20}^{+0.34} \text{ keV}, R_{\text{MCD}} = 56_{-27}^{+46} \text{ km}, kT_{\text{BB}} = 1.43_{-0.35}^{+1.76} \text{ keV}, R_{\text{BB}} = 14.6_{-11.3}^{+10.6} \text{ km}$	0.93(55)	166+10	166+13
25	MCD+BB	$0.0^{+11.2}$	$kT_{\text{MCD}} = 0.46^{+0.23}_{-0.18} \text{ keV}, R_{\text{MCD}} = 100^{+238}_{-51} \text{ km}, kT_{\text{BB}} = 1.11^{+0.32}_{-0.16} \text{ keV}, R_{\text{BB}} = 26.7^{+10.4}_{-10.8} \text{ km}$	1.17(72)	184^{+11}_{-14}	184^{+29}_{-11}
35	MCD+BB	$0.0^{+5.8}$	$kT_{\text{MCD}} = 0.52^{+0.24}_{-0.18} \text{ keV}, R_{\text{MCD}} = 77^{+98}_{-21} \text{ km}, kT_{\text{BB}} = 1.22^{+0.59}_{-0.22} \text{ keV}, R_{\text{BB}} = 18.4^{+9.4}_{-10.0} \text{ km}$	0.74(45)	137^{+11}_{-11}	137^{+12}_{-10}
68	MCD+BB	$1.7^{+5.6}$	$kT_{\text{MCD}} = 0.42^{+0.11}_{-0.09} \text{ keV}, R_{\text{MCD}} = 154^{+128}_{-59} \text{ km}, kT_{\text{BB}} = 1.24^{+0.21}_{-0.15} \text{ keV}, R_{\text{BB}} = 24.1^{+6.4}_{-5.9} \text{ km}$	0.82(84)	231^{+15}_{-14}	239^{+22}_{-16}
200	MCD+BB	$0.0^{+1.0}$	$kT_{\text{MCD}} = 0.62^{+0.35}_{-0.15} \text{ keV}, R_{\text{MCD}} = 106^{+60}_{-54} \text{ km}, kT_{\text{BB}} = 1.16^{+0.38}_{-0.14} \text{ keV}, R_{\text{BB}} = 41.5^{+13.8}_{-21.3} \text{ km}$	0.96(165)	556^{+21}_{-21}	556^{+21}_{-21}
212	MCD+BB	$0.0^{+5.8}$	$kT_{\rm MCD} = 0.56^{+0.18}_{-0.15}~{\rm keV}, R_{\rm MCD} = 113^{+100}_{-44}~{\rm km}, kT_{\rm BB} = 1.15^{+0.21}_{-0.13}~{\rm keV}, R_{\rm BB} = 36.0^{+10.1}_{-11.4}~{\rm km}$	0.91(123)	416^{+16}_{-20}	416^{+30}_{-16}
8	MCD+BB	$0.0^{+0.6}$	$kT_{\text{MCD}} = 1.70(\text{f}) \text{ keV}, R_{\text{MCD}} = 13.1_{-0.3}^{+0.3} \text{ km}, kT_{\text{BB}} = 2.50(\text{f}) \text{ keV}, R_{\text{BB}} = 0.0^{+1.6} \text{ km}$	1.37(57)	165 ⁺⁷	165 ⁺⁷ ₋₇
25	MCD+BB	$0.0^{+0.6}$	$kT_{\text{MCD}} = 1.70(\text{f}) \text{ keV}, R_{\text{MCD}} = 13.8^{+0.3}_{-0.4} \text{ km}, kT_{\text{BB}} = 2.50(\text{f}) \text{ keV}, R_{\text{BB}} = 0.1^{+2.6} \text{ km}$	1.38(75)	183^{+11}_{-7}	183^{+11}_{-7}
35	MCD+BB	$0.0^{+0.6}$	$kT_{\text{MCD}} = 1.70(\text{f}) \text{ keV}, R_{\text{MCD}} = 12.0^{+0.3}_{-0.3} \text{ km}, kT_{\text{BB}} = 2.50(\text{f}) \text{ keV}, R_{\text{BB}} = 0.0^{+1.5} \text{ km}$	1.32(47)	137^{+6}_{-6}	137^{+6}_{-6}
68	MCD+BB	$0.0^{+0.4}$	$kT_{\text{MCD}} = 1.70(\text{f}) \text{ keV}, R_{\text{MCD}} = 15.2_{-0.4}^{+0.4} \text{ km}, kT_{\text{BB}} = 2.50(\text{f}) \text{ keV}, R_{\text{BB}} = 0.1^{+2.2} \text{ km}$	1.73(86)	220^{+9}_{-8}	220^{+9}_{-8}
200	MCD+BB	$0.0^{+0.4}$	$kT_{\text{MCD}} = 1.70(\text{f}) \text{ keV}, R_{\text{MCD}} = 24.3_{-0.4}^{+0.4} \text{ km}, kT_{\text{BB}} = 2.50(\text{f}) \text{ keV}, R_{\text{BB}} = 0.1^{+2.4} \text{ km}$	1.05(167)	565^{+13}_{-14}	565^{+13}_{-13}
212	MCD+BB	$0.0^{+0.4}$	$kT_{\text{MCD}} = 1.70(\text{f}) \text{ keV}, R_{\text{MCD}} = 21.0^{+0.4}_{-0.4} \text{ km}, kT_{\text{BB}} = 2.50(\text{f}) \text{ keV}, R_{\text{BB}} = 0.1^{+1.8} \text{ km}$	1.14(125)	422^{+12}_{-12}	422^{+12}_{-12}

Note. Columns: (1) master source unique index; (2) the spectral model; (3) intrinsic column density; (4) other spectral parameters (R_{BB} is the apparent source radius from the BB normalization $N_{BB} \equiv ((R_{BB}/\text{km})/(D/10\text{kpc}))^2$; refer to Table 6 for the meanings of other parameters); (5) the reduced χ^2 and the degrees of freedom (only for fits to spectra binned to have a minimum of 20 counts and using the χ^2 statistic); (7)–(8) the absorbed (but corrected for Galactic absorption) and unabsorbed 0.3–8 keV luminosity (assuming isotropic emission or a disk inclination of 60°), respectively. All errors are at the 90% confidence level.

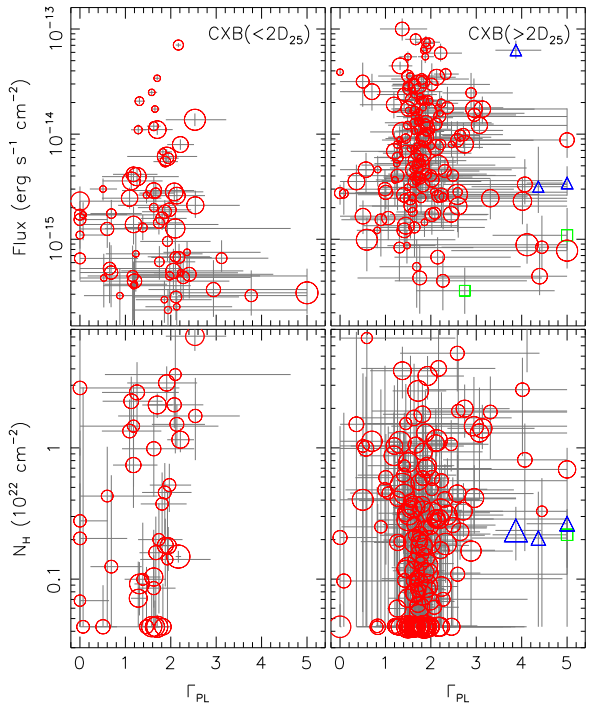


Figure 7. Similar to Figure 5 but for the PL fits to candidate CXB sources. Sources inside and outside $2D_{25}$ are plotted in the left and right panels, respectively. The bottom panels for $N_{\rm H}$ vs. $\Gamma_{\rm PL}$ only show sources with $L_{\rm X} > 8 \times 10^{-16}~{\rm erg~s}^{-1}~{\rm cm}^{-2}$. Three candidate coronally active stars (triangles in the right panels) are also included. Two faint soft sources (squares in the right panels) could be from hot gas emission of optically bright galaxies.

(2004) reported two sources (their S22 and S32) in two GCs (Bo91 and Bo158, respectively) in M31 having $\Gamma_{PL} \sim 0.6$ –0.8 and the 0.3–10 keV luminosity $\sim (0.6-1.8)\times 10^{38}$ erg s⁻¹. These two sources showed a spectral cutoff of ~4-8 keV (our source showed no cutoff below 12 keV at the 90% confidence level). It is not clear whether these sources have a common nature. Burke et al. (2013) suggested their S48 as a highly magnetized NS as seen in normal accreting X-ray pulsars (instead of millisecond X-ray pulsars), which typically have $\Gamma_{PL}\lesssim 1,$ cutoff energies around 20 keV, and luminosities $\gtrsim\!10^{36}\,erg\,s^{-1}$ (White et al. 1983). Considering that such objects normally show coherent pulsations, we searched for them for our source by creating power density spectra for each observation (refer to Lin et al. 2014 for the procedure). We found no detection above the 99% significance level in any observation from the timescale of the whole observation length up to the Nyquist frequencies (0.62 Hz for observations 1–3 and 0.64 Hz for observations 4–11). It is possible that its pulsation period is shorter than the readout frame time or that the pulsation is not strong enough to be detected with the current data. Most normal accreting X-ray pulsars are high-mass X-ray binaries, with only a few known to be LMXBs (Bildsten et al. 1997). Given the coincidence with a GC, S223 is more likely to be a LMXB if it is a normal accreting X-ray pulsar.

We note that the hard X-ray source in Bo158 in M31 showed periodic dips occasionally and thus probably has a high inclination (Trudolyubov et al. 2002; Trudolyubov & Priedhorsky 2004). Therefore we speculate an alternative explanation for the hard spectra of these sources: they might have high inclination angles, which suppress the observed disk emission

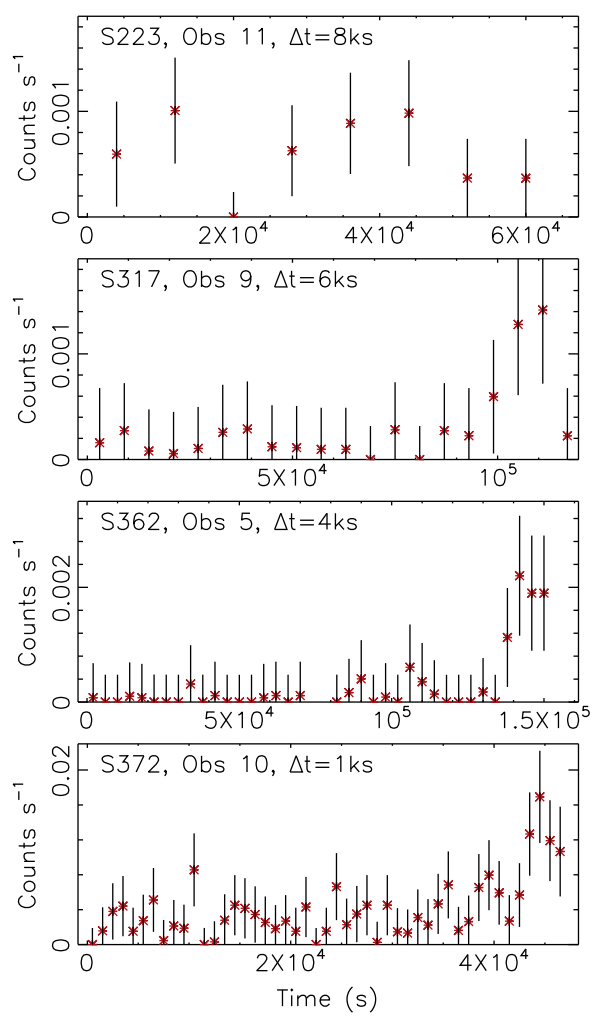


Figure 8. Light curves of some sources with interesting variability, with Gehrels errors (Gehrels 1986) shown. The top panel is for S223, which is a candidate NS LMXB with a strong magnetic field or a high inclination in a GC, in observation 11, showing significant short-term variability. The bottom three panels are for three coronally active star candidates in observations showing sign of flares. The bin size Δt of each light curve is annotated in each panel.

and enhance the observed boundary layer emission and thus cause the hard X-ray spectra (but the inclination should not be too high for the boundary layer to be strongly obscured by the disk). Limited by statistics, we cannot determine whether the short-term variability of our source S223 in observation 11 is due to dipping.

4. DISCUSSION

4.1. The NS LMXB Soft State Track and The New Source Identification Scheme

Except for some very soft outliers, which should be strong BHCs in the thermal state, the majority of our bright sources appear hard in the *Chandra* bandpass (0.3–8 keV). They could be BHBs in the hard state or NS LMXBs in the soft state. The spectra of NS LMXBs in the soft state can appear hard in this energy band due to the hot boundary layer emission. Differentiating between the above two scenarios is nontrivial based on the narrow-band spectra in hand. The method that we

adopted is to compare the collective spectral properties of our sources with the spectral evolution of three representative Galactic X-ray binaries based on simple PL and MCD fits. We found that most of our sources fall on a narrow track in the $L_{\rm X}$ versus $\Gamma_{\rm PL}$ and $L_{\rm X}$ versus $kT_{\rm MCD}$ plots, exhibiting harder spectra at higher luminosity below $L_{\rm X}\sim 7\times 10^{37}\,{\rm erg\,s^{-1}}$, but a relatively constant spectral shape above this luminosity. Such spectral evolution is close to that expected for NS LMXBs in the soft state in the *Chandra* bandpass. Therefore, we identify the track as the NS LMXB soft-state track, in which sources below $L_{\rm X}\sim 7\times 10^{37}\,{\rm erg\,s^{-1}}$ are most likely atolls in the soft state and sources above this luminosity are Z sources.

Our sample of candidate LMXBs in NGC 3115 also includes some hard sources at low luminosities. Although we believe that they should be dominated by NS LMXBs, the possibility of some being BHBs (even AGNs) cannot be ruled out. Therefore, our list of BHBs should be conservative, only including the 10 strong BHCs that were identified based on their very soft spectra. Restricting our search to $(0.046-1.0)D_{25}$ and above 10^{37} erg s⁻¹, we found one persistent BHC out of 23 GC LMXBs and nine BHCs (five persistent and four transient) out of 59 field LMXBs. Therefore, we found a much larger fraction of BHBs in the field than in GCs, as seen in our Galaxy. We have identified four BHCs out of 11 field transients. This is more abundant than the simulations by Fragos et al. (2008) (<10% for transients above 10^{37} erg s⁻¹). Our discovery of five persistent BHCs in the field with $L_{\rm X} \gtrsim 10^{37}\,{\rm erg\,s^{-1}}$ was also not predicted by Fragos et al. (2008).

X-ray sources in the old populations in other galaxies seem to show similar spectral properties to those of our sources and can thus be identified in the same way. Trudolyubov & Priedhorsky (2004) fitted the XMM-Newton (using the 0.3–10 keV band) and *Chandra* (using the 0.5–7 keV band) spectra of 31 bright GC LMXBs in M31 with an absorbed PL. Their sources had the 0.3-10 keV luminosity L_X in the range of $\sim 10^{36} - 10^{39} \,\mathrm{erg \, s^{-1}}$. In the $L_{\rm X}$ versus $\Gamma_{\rm PL}$ plot (their Figure 6), we can see that most of their sources reside in the NS LMXB soft-state track and thus should be atolls in the soft state and Z sources following our identification scheme, except some hard sources at low luminosities, which could be NS (most likely) or BH LMXBs in the hard state. Trudolyubov & Priedhorsky (2004) also argued that most of their sources, almost all being persistent, should be NS LMXBs, based on the similarity of their spectral properties and long-term variability to those of luminous persistent X-ray binaries in our Galaxy (they are mostly NS LMXBs). However, in their fits to the three brightest $(L_{\rm X}>10^{38}~{\rm erg~s^{-1}})$ sources with the MCD+BB model, two have $kT_{\text{MCD}} \lesssim 1 \text{ keV}$, which seems too low for Z sources, as will be discussed below.

In the study of X-ray binaries in Centaurus A observed by *Chandra*, Burke et al. (2013) also obtained the $L_{\rm X}$ versus $\Gamma_{\rm PL}$ plot and the $L_{\rm X}$ versus $kT_{\rm MCD}$ plot (their Figures 2 and 3, respectively), but for only some bright sources (0.5–10 keV luminosity $L_{\rm X}$ in the range of $\sim 10^{37}$ –4 $\times 10^{38}$ erg s⁻¹). They tried to determine whether the source spectra were dominated by an MCD or PL based on the behavior of the inferred column density. Their method followed Brassington et al. (2010), who came up with this method based on simulations of typical BHB spectra. We prefer our source identification scheme, which is based on the spectral behavior of both NS and BH LMXBs. Almost all 17 sources in the $L_{\rm X}$ versus $\Gamma_{\rm PL}$ plot that Burke et al.

(2013) found to be PL dominated are in the NS LMXB soft-state track. Among the 16 sources in the $L_{\rm X}$ versus $kT_{\rm MCD}$ plot that Burke et al. (2013) found to be MCD dominated, 12 are in the NS LMXB soft-state track, while the other four have very soft spectra ($kT_{\rm MCD} \lesssim 1\,{\rm keV}$) and are probably BHBs in the thermal state. Burke et al. (2013) generally gave consistent source identifications, which were mostly based on the disk temperature from the MCD fits only, and our more detailed comparison with Galactic NS LMXBs makes the identification of the source nature and spectral state more convincing.

4.2. Comparison with The Double Thermal Model Source Identification Method

Given that Lin et al. (2007, 2009, 2010, 2012a) successfully fitted thousands of NS LMXB soft-state spectra with the double thermal model (MCD+BB), plus a weak Comptonized component when necessary, Barnard et al. (2013) applied the double thermal model to 35 sources in M31 showing bright hard spectra and found them to be BHCs because their bestfitting parameters were significantly outside the space occupied by NS LMXBs. In particular, they found that the disk temperatures of their BHCs from the fits with the double thermal model were systematically lower ($kT_{MCD} \lesssim 1.0 \text{ keV}$) than those of typical NS LMXB soft-state spectra $(kT_{\rm MCD} \gtrsim 1.0 \, {\rm keV})$, and the BB fractions of the 2–10 keV flux were also larger (>65% versus <50%). Barnard et al. (2014) expanded their work and found 15 more BHCs (i.e., 50 in total). These 50 BHCs include 15 GC sources, 12 of which were included in Trudolyubov & Priedhorsky (2004). Based on our source identification scheme, however, these 15 BHCs (two of which are transients) in GCs should be NS LMXBs. For the other 35 non-GC sources, most should be NS LMXBs too, except for about six sources with very soft spectra, which should be BHCs.

We also tried to fit the double thermal model to our bright sources with $L_{\rm X} > 4 \times 10^{37}\,{\rm erg\,s^{-1}}$. There are 33 (14 in GCs and 19 in the field), excluding the soft BHCs that we have identified. We found that they all have $kT_{\rm MCD} < 1\,{\rm keV}$, and 27 have an upper error of $kT_{\rm MCD}$ at the 90% confidence level <1 keV. Following Barnard et al. (2013) and Barnard et al. (2014), this would indicate that almost all bright sources with $L_{\rm X} > 4 \times 10^{37}\,{\rm erg\,s^{-1}}$ in NGC 3115 are BHCs, which seems very unlikely considering that BHBs are expected to be much rarer than NS LMXBs in an early-type galaxy like NGC 3115 (Fragos et al. 2008).

We note that we are using a narrower and softer energy band and have sources subject to much less absorption than Lin et al. (2007, 2009, 2010, 2012a). These differences could cause problems if the double thermal model is directly applied to our sources. Thus, we estimated the possible systematic errors arising from the use of a narrow energy band. Using the brightest observation (suz4) of 4U 1705-44 in Lin et al. (2010), which has $kT_{MCD} = 1.66 \text{ keV}$ and a BB fraction of 30% in 2-10 keV, we simulated 200 spectra with Galactic absorption in the direction of NGC 3115 and then fitted them with the double thermal model with the column density fixed at the Galactic value. We obtained a median of $kT_{\rm MCD} = 1.48^{+0.29}_{-0.74} \, {\rm keV}$ (the error bar corresponds to the 90% confidence level in the sense that the upper and lower error bars each include 45% of the fits). We also found that 77% and 46% of the simulated spectra have the best-fitting BB fraction in 2–10 keV larger than 30% (the BB fraction of

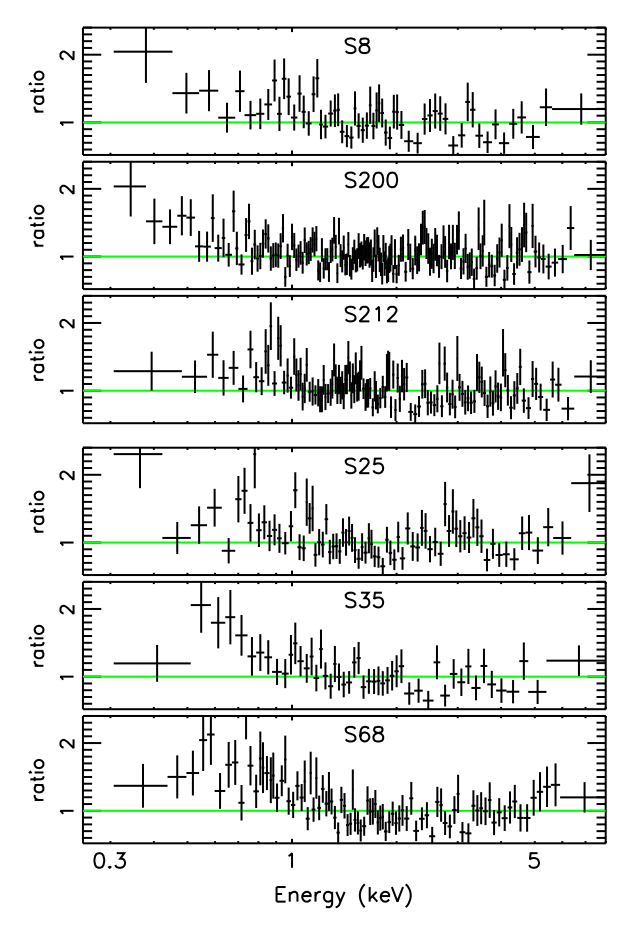


Figure 9. Residuals of fits to sample LMXBs with the double thermal model, with the temperatures of the thermal components fixed at values typical of Z sources ($kT_{MCD} = 1.7 \text{ keV}$ and $kT_{BB} = 2.5 \text{ keV}$).

suz4) and 50%, respectively. These simulation results indicate that the use of the limited energy band could systematically infer a lower disk temperature and more BB contribution in 2–10 keV than expected.

We investigated whether the sources could be fitted well if the temperatures of the double thermal components are fixed at values typically seen in NS LMXBs. We concentrate on six bright sources—the two brightest persistent field LMXBs (S25 and S68), the brightest transient field LMXB (S35), the two brightest persistent LMXBs in GCs (S200 in a blue GC and S212 in a red GC), and the brightest transient GC LMXB (S8); see Table 7. Because they all have near or super-Eddington luminosity $(L_{\rm X} > 10^{38} \, {\rm erg \, s^{-1}}, \, {\rm brighter} \, {\rm than} \, {\rm the} \, {\rm brightest}$ observation (suz4) of 4U 1705-44 in Lin et al. 2010), we expect them to be Z sources if they are NS LMXBs. Then they should have $kT_{\rm MCD}$ around 1.7 keV and $kT_{\rm BB}$ around 2.5 keV based on the double thermal model (Lin et al. 2009, 2012a). Therefore, we also fitted them with the temperatures of the thermal components fixed at these values. The fit results are given in Table 7, and the residuals are shown in Figure 9. The fits overall seem fine, but below around 1 keV we can see a clear systematic soft excess in all sources.

One possible explanation of such a soft excess is that the real disk spectrum is broader than the simple MCD description. A detailed disk model should carefully calculate radiative transfer through the vertical structure of the disk and account for the relativistic smearing. This is implemented in the relativistic disk model *bhspec*, which indicates that the real disk spectrum

should have excess emission relative to the MCD description by more than 10% at low energies (Davis et al. 2005, 2006; Davis & Hubery 2006; Kubota et al. 2010). Because NSs tend to have a hotter disk, resulting in more of the low-energy part of the disk spectrum to be observed in the *Chandra* bandpass than would be the case for BHs, the soft excess of the real disk spectrum relative to the MCD description is expected to be more obvious for NSs than for BHs. Such soft excess was not seen by Lin et al. (2007, 2009, 2010, 2012a) because they used spectra above 1 keV and the sources that they studied had much higher absorption than the sources studied here. However, bhspec has two limitations, preventing us from applying it to our sources. One is that it is a table model for the BH accretion disk with the minimum BH mass $M_{\rm BH}$ of $3M_{\odot}$, which is not suitable for the accretion disk around NSs. In any case, the model assumes that the inner disk radius is at the ISCO, which is not necessarily the case for our luminous sources, whose inner disk could reach the local Eddington limit and thus be truncated outside the ISCO (Lin et al. 2009).

Given this possible soft excess problem, we did not use the MCD+BB fits to find more BHCs, other than those identified in Section 3.3 based on their very soft spectra, which is a characteristic that is not seen in NS LMXBs.

5. CONCLUSIONS

We studied LMXBs detected in NGC 3115 using the Megasecond *Chandra* XVP observations. Including three previous observations, the total exposure time is 1.1 Ms. Thus NGC 3115 is one of *Chandra*'s best observed galaxies. In total we have 136 candidate LMXBs in the field and 49 in GCs detected above 2σ , with $L_{\rm X}$ in the range of $\sim 10^{36}$ to 10^{39} erg s⁻¹. We calculated the long-term variability for all sources and identified 13 transient candidates whose long-term variability factors are >5. Excluding these transients, the sources have long-term variability overall, decreasing with increasing luminosity, at least at $L_{\rm X} \gtrsim 2 \times 10^{37}$ erg s⁻¹.

We carried out simple fits to our sources using singlecomponent models (a simple PL or MCD). We found that in the L_X versus Γ_{PL} and L_X versus kT_{MCD} plots a majority of our sources fall on a narrow track, showing harder spectra at higher luminosity below $L_{\rm X}\sim7\times10^{37}\,{\rm erg\,s^{-1}}$ but relatively constant spectral shape ($\Gamma_{\rm PL}\sim1.5~{\rm or}~kT_{\rm MCD}\sim1.5~{\rm keV}$) above this luminosity. Because our simulations showed that the Galactic NS LMXBs in the soft state show similar spectral evolution in the Chandra bandpass, we identified the track as the NS LMXB soft-state track and suggested sources below $L_{\rm X} \sim 7 \times 10^{37} \, {\rm erg \, s^{-1}}$ as atolls in the soft state and sources above this luminosity as Z sources. However, the spectra of our sources seem to show systematic soft excess relative to the double thermal (MCD+BB) modeling by Lin et al. (2007, 2009, 2010, 2012a) of Galactic NS LMXBs. One explanation for this is that the real disk spectrum has excess soft emission relative to the MCD description. This is expected from detailed simulations involving careful calculation of radiative transfer through the vertical structure of the disk and accounting for the relativistic smearing (Davis et al. 2005; Davis & Hubeny 2006).

Ten sources are significantly softer than others at similar luminosities and are strong BHCs in the thermal state. Five of those are persistent (one in a blue GC), and the other five are transient.

Some special objects were discovered. S198 is the only transient BHC whose outburst was covered relatively well by our observations. The source displayed clear spectral change during the outburst. In the peak, it is consistent with a BHC of $M_{\rm BH} \sim 6~M_{\odot}$ in the thermal state with $kT_{\rm MCD} = 0.78 \pm 0.07$ keV and L_X at 0.12 Eddington luminosity. The spectrum during the rise and decay was much softer, with $kT_{\rm MCD} = 0.17 \pm 0.05$ keV and the disk flux fraction >63% (the 90% upper limit); L_X was at ~ 0.008 Eddington luminosity, indicating the possible presence of a strong thermal disk at a very low Eddington ratio in a BHB. The source could be in the transitional or hard state. S109 is a persistent SSS, with $kT_{\rm BB}=86^{+4}_{-12}$ eV and $L_{\rm BB,bol}=0.8^{+2.2}_{-0.2}\times10^{38}\,\rm erg\,s^{-1}$, and can be explained as due to steady nuclear burning on the surface of a WD. S223 is a persistent luminous source in a GC with very hard $(\Gamma = 0.6 \pm 0.1)$ X-ray spectra source. It is a candidate NS LMXB with a high magnetic field or a high inclination.

We thank the anonymous referee for the helpful comments. The work is supported by *Chandra* XVP grant GO2-13104X. This material is based upon work supported in part by the National Science Foundation under Grants AST-1211995 and AST-1308124. This material is based upon work supported in part by *HST*-GO-12759.02 A and *HST*-GO-12759.12 A. G.R.S. acknowledges support from an NSERC Discovery Grant.

REFERENCES

```
Arnaud, K. A. 1996, in ASP Conf. Ser. 101, Astronomical Data Analysis
  Software and Systems V, ed. G. H. Jacoby & J. Barnes (San Francisco, CA:
   ASP), 17
Arnold, J. A., Romanowsky, A. J., Brodie, J. P., et al. 2011, ApJL, 736, L26
Barnard, R., Garcia, M. R., & Murray, S. S. 2013, ApJ, 770, 148
Barnard, R., Garcia, M. R., Primini, F., & Murray, S. S. 2014, ApJ, 791, 33
Bautz, M. W., Pivovaroff, M., Baganoff, F., et al. 1998, Proc. SPIE, 3444, 210
Bildsten, L., Chakrabarty, D., Chiu, J., et al. 1997, ApJS, 113, 367
Bradt, H. V., Rothschild, R. E., & Swank, J. H. 1993, A&AS, 97, 355
Brassington, N. J., Fabbiano, G., Blake, S., et al. 2010, ApJ, 725, 1805
Brassington, N. J., Fabbiano, G., Zezas, A., et al. 2012, ApJ, 755, 162
Burke, M. J., Raychaudhury, S., Kraft, R. P., et al. 2013, ApJ, 766, 88
Chen, W., Shrader, C. R., & Livio, M. 1997, ApJ, 491, 312
Davis, S. W., Blaes, O. M., Hubeny, I., & Turner, N. J. 2005, ApJ, 621, 372
Davis, S. W., Done, C., & Blaes, O. M. 2006, ApJ, 647, 525
Davis, S. W., & Hubeny, I. 2006, ApJS, 164, 530
de Vaucouleurs, G., de Vaucouleurs, A., Corwin, H. G., Jr. et al. (ed.) 1991,
   Third Reference Catalogue of Bright Galaxies (New York: Springer)
Di Stefano, R., Kong, A., & Primini, F. A. 2010, NewAR, 54, 72
Done, C., & Gierliński, M. 2003, MNRAS, 342, 1041
Done, C., Gierliński, M., & Kubota, A. 2007, A&ARv, 15, 1
Evans, I. N., Primini, F. A., Glotfelty, K. J., et al. 2010, ApJS, 189, 37
Fragos, T., Kalogera, V., Belczynski, K., et al. 2008, ApJ, 683, 346
Freeman, P. E., Kashyap, V., Rosner, R., & Lamb, D. Q. 2002, ApJS, 138, 185
Fridriksson, J. K., Homan, J., & Remillard, R. A. 2015, arXiv:1504.00022
Galloway, D. K., Morgan, E. H., Krauss, M. I., Kaaret, P., & Chakrabarty, D.
  2007, ApJL, 654, L73
Galloway, D. K., Muno, M. P., Hartman, J. M., Psaltis, D., & Chakrabarty, D.
  2008, ApJS, 179, 360
Gehrels, N. 1986, ApJ, 303, 336
Georgakakis, A., Nandra, K., Laird, E. S., Aird, J., & Trichas, M. 2008,
      IRAS, 388, 1205
Gierliński, M., Done, C., & Page, K. 2008, MNRAS, 388, 753
Gregory, P. C., & Loredo, T. J. 1992, ApJ, 398, 146
Greiner, J. 2000, NewA, 5, 137
Haberl, F., & Titarchuk, L. 1995, A&A, 299, 414
Hasinger, G., & van der Klis, M. 1989, A&A, 225, 79
Homan, J., & Belloni, T. 2005, Ap&SS, 300, 107
Homan, J., Kaplan, D. L., van den Berg, M., & Young, A. J. 2009, ApJ,
  692. 73
Homan, J., van der Klis, M., Fridriksson, J. K., et al. 2010, ApJ, 719, 201
Inogamov, N. A., & Sunyaev, R. A. 1999, AstL, 25, 269
```

```
Irwin, J. A. 2006, MNRAS, 371, 1903
Irwin, J. A., Athey, A. E., & Bregman, J. N. 2003, ApJ, 587, 356
Jennings, Z. G., Strader, J., Romanowsky, A. J., et al. 2014, AJ, 148, 32
Kalberla, P. M. W., Burton, W. B., Hartmann, D., et al. 2005, A&A,
  440, 775
Kim, E., Kim, D.-W., Fabbiano, G., et al. 2006, ApJ, 647, 276
Kim, M., Kim, D.-W., Wilkes, B. J., et al. 2007, ApJS, 169, 401
Kubota, A., Done, C., Davis, S. W., et al. 2010, ApJ, 714, 860
Kubota, A., Tanaka, Y., Makishima, K., et al. 1998, PASJ, 50, 667
Li, J., Kastner, J. H., Prigozhin, G. Y., et al. 2004, ApJ, 610, 1204
Lin, D., Irwin, J. A., Wong, K.-W., et al. 2015, ApJ, 808, 20 (Paper III)
Lin, D., Remillard, R. A., & Homan, J. 2007, ApJ, 667, 1073
Lin, D., Remillard, R. A., & Homan, J. 2009, ApJ, 696, 1257
Lin, D., Remillard, R. A., & Homan, J. 2010, ApJ, 719, 1350
Lin, D., Remillard, R. A., Homan, J., & Barret, D. 2012a, ApJ, 756, 34
Lin, D., Webb, N. A., & Barret, D. 2012b, ApJ, 756, 27
Lin, D., Webb, N. A., & Barret, D. 2014, ApJ, 780, 39
Maccarone, T. J. 2003, A&A, 409, 697
Maccarone, T. J., & Coppi, P. S. 2003, MNRAS, 338, 189
Maccarone, T. J., Kundu, A., & Zepf, S. E. 2003, ApJ, 586, 814
Maccarone, T. J., Long, K. S., Knigge, C., Dieball, A., & Zurek, D. R. 2010,
   MNRAS, 406, 2087
Makishima, K., Kubota, A., Mizuno, T., et al. 2000, ApJ, 535, 632
McClintock, J. E., & Remillard, R. A. 2006, in Compact Stellar X-ray Sources,
   ed. W. Lewin & M. van der Klis (Cambridge: Cambridge Univ. Press)
Miller, J. M., Homan, J., Steeghs, D., et al. 2006, ApJ, 653, 525
```

```
Miyamoto, S., Kitamoto, S., Hayashida, K., & Egoshi, W. 1995, ApJL,
  442, L13
Monet, D. G., Levine, S. E., Canzian, B., et al. 2003, AJ, 125, 984
Park, T., Kashyap, V. L., Siemiginowska, A., et al. 2006, ApJ, 652, 610
Popham, R., & Sunyaev, R. 2001, ApJ, 547, 355
Pota, V., Forbes, D. A., Romanowsky, A. J., et al. 2013, MNRAS, 428, 389
Remillard, R. A., & McClintock, J. E. 2006, ARA&A, 44, 49
Rykoff, E. S., Miller, J. M., Steeghs, D., & Torres, M. A. P. 2007, ApJ,
  666, 1129
Sánchez-Blázquez, P., Gorgas, J., Cardiel, N., & González, J. J. 2006, A&A,
  457, 809
Shakura, N. I., & Sunyaev, R. A. 1973, A&A, 24, 337
Soleri, P., Fender, R., Tudose, V., et al. 2010, MNRAS, 406, 1471
Tonry, J. L., Dressler, A., Blakeslee, J. P., et al. 2001, ApJ, 546, 681
Trudolyubov, S., & Priedhorsky, W. 2004, ApJ, 616, 821
Trudolyubov, S. P., Borozdin, K. N., Priedhorsky, W. C., et al. 2002, ApJL,
  581, L27
van der Klis, M. 2006, in Compact Stellar X-ray Sources, ed. W. Lewin &
  M. van der Klis (Cambridge: Cambridge Univ. Press)
van Paradijs, J., & McClintock, J. E. 1995, X-ray Binaries, ed. W. H. G. Lewin,
  J. van Paradijs & E. P. J. van den Heuval (Cambridge: Cambridge Univ.
Weisskopf, M. C., Brinkman, B., Canizares, C., et al. 2002, PASP, 114, 1
White, N. E., Swank, J. H., & Holt, S. S. 1983, ApJ, 270, 711
Wong, K.-W., Irwin, J. A., Shcherbakov, R. V., et al. 2014, ApJ, 780, 9
Wong, K.-W., Irwin, J. A., Yukita, M., et al. 2011, ApJL, 736, L23
```